Front. Struct. Civ. Eng.
https://doi.org/10.1007/s11709-019-0605-8

RESEARCH ARTICLE

Wavelet-based iterative data enhancement for implementation in purification of modal frequency for extremely noisy ambient vibration tests in Shiraz-Iran

Hassan YOUSEFI[a*], Alireza TAGHAVI KANI[b], Iradj MAHMOUDZADEH KANI[b], Soheil MOHAMMADI[a]

[a] *High Performance Computing Lab, School of Civil Engineering, Faculty of Engineering, University of Tehran, Tehran, Iran*
[b] *School of Civil Engineering, Faculty of Engineering, University of Tehran, Tehran, Iran*
[*] *Corresponding author. E-mail: hyosefi@ut.ac.ir*

ABSTRACT The main purpose of the present study is to enhance high-level noisy data by a wavelet-based iterative filtering algorithm for identification of natural frequencies during ambient wind vibrational tests on a petrochemical process tower. Most of denoising methods fail to filter such noise properly. Both the signal-to-noise ratio and the peak signal-to-noise ratio are small. Multiresolution-based one-step and variational-based filtering methods fail to denoise properly with thresholds obtained by theoretical or empirical method. Due to the fact that it is impossible to completely denoise such high-level noisy data, the enhancing approach is used to improve the data quality, which is the main novelty from the application point of view here. For this iterative method, a simple computational approach is proposed to estimate the dynamic threshold values. Hence, different thresholds can be obtained for different recorded signals in one ambient test. This is in contrast to commonly used approaches recommending one global threshold estimated mainly by an empirical method. After the enhancements, modal frequencies are directly detected by the cross wavelet transform (XWT), the spectral power density and autocorrelation of wavelet coefficients. Estimated frequencies are then compared with those of an undamaged-model, simulated by the finite element method.

KEYWORDS ambient vibration test, high level noise, iterative signal enhancement, wavelet, cross and autocorrelation of wavelets

1 Introduction

Ambient vibration tests are usually used for: damage detections [1,2]; modal parameter identifications in health monitoring studies [3–9]; assessment of real time conditions [3,4,10–22]; and vibration controls [23]. The ambient vibration tests are fast and cheap, and require no excitation equipment and can be used for different structures and infrastructures [24,25]. In these tests, the source of loading can be environmental or natural excitation; some common examples are: wind [3,16,17,19,20], traffic loads [26], and small to moderate earthquakes [27]. The ambient vibration tests mainly estimate the linear response of (damaged) structures, since the magnitude of loading is small. The *in situ* tests are interesting [28,29] because they are directly performed on (partially damaged) full-scale structures to control their performance (deviations from initial conditions). However, the identification of system parameters (i.e., modal frequencies, service condition's modal damping and mode shapes) is nearly challenging in ambient vibrations, due to non-stationary responses, nonlinear signals and high-level of noise in recorded data [30,31]. The signal-to-noise ratios (*SNR*s) of these recorded signals have significant effects on the accuracy of parameter identification phase [32]. For this reason, noise effects on modal identifications have been studied for different approaches [33–36].

For removing/curing noise effects in recorded data in a multiresolution framework, wavelet theories, which are fast with a strong mathematical background, have been developed. Wavelet transforms (WTs) study data in the time-frequency representation with different

Article history: Received Feb 10, 2019; Accepted Mar 24, 2019

decomposition levels and resolution accuracy in a non-parametric approach using only the output data [3,4,10–13,18,19,27,37–42]. For high level of noise, however, this powerful transform has its own shortcomings [43].

Two general denoising approaches can be addressed in the framework of multiresolution analysis (MRA): one-step [44–50] and iterative techniques [51–57]. In the former, one stage of MRA allows for noise to be estimated and removed from the data. In the iterative approach, successive refinements of the data are used for estimation of the denoised data. This iterative scheme can filter noise in a step-by-step approach to clear or enhance the data. It should be noted that, in signals with high-level of noise, it is almost impossible to completely eliminate (filter) the noise.

The iterative denoising algorithm was originally proposed by Starck and Bijaoui [57] and Coifman and Wickerhauser [51,52]; and then it was followed by Hadjileontiadis et al. [53,54] and Ranta et al. [55,56]. In each iteration, information with coherent structures in different resolution levels is selected and the remaining data are assumed as noise in the next iteration. Since the physical information is gathered layer by layer from the noise residual, the approach is also known as the "peeling off successive layers" scheme [51,52]. The iterative method assumes that large wavelet coefficients contain physical information. These coefficients are detected based on a (predefined) threshold in each resolution level: known as the level-dependent thresholds. Each threshold in each resolution level can be in accordance with the deviation of wavelet coefficients in that resolution (a level-depending thresholding).

The thresholds for the iterative scheme can be chosen empirically or based on some criteria [53]. In this study, a simple data-dependent criterion is explained based on peak signal-to-noise ratio (*PSNR*) and *SNR*. This approach leads to dynamic threshold values for different recorded data obtained even in an ambient vibration test. This leads to a more flexible noise estimation method in comparison to commonly used approaches employing one constant threshold for all data. To control the stochastic feature of the estimated noises, the time-frequency representation of estimated noises (by the iterative enhancing method) are presented and studied for some recorded data. This feature confirms effectiveness of the estimated dynamic thresholds and the iterative method.

For noisy information with small values of *SNR*, the importance of the iterative denoising approach is studied and confirmed by comparing the results with:

1) The one-step MRA-based denoising scheme: This comparison is performed for different decomposition levels and wavelet families. In computations, wavelet thresholds are those obtained by both theoretical and empirical approaches [58].

2) The variational-based filtering approach with different constraints [58].

Neither the one-step MRA-based denoising nor the variational-based one can properly enhance high-level noisy recorded data gathered during the ambient vibration tests.

After the signal-enhancement step, other MRA-based approaches are used here to improve the detection power of physical features (without stochastic properties). After the enhancement step, it is still a challenging task to determine physical features in the enhanced data. In this regard, detections are performed by:

1) The concept of the XWT [45,59], and the corresponding spectral power. The XWT analysis and the corresponding spectral power are simultaneously used for frequency detections. Responses with both the continuity pattern in time (controlled by XWT) and considerable energies in the spectral power can be assumed to include physical phenomena.

2) Autocorrelation of wavelet coefficients: by autocorrelation of wavelet coefficients, the repeating patterns of different scales can be detected for different resolution levels in time [60,61]. This transform is especially important for capturing the repeating features of weakly excited responses (e.g., higher modes of a structure with small participations) which cannot be detected by the above-mentioned transforms.

For data with high-level of noise, in general, the noises affect all time-scales in the scalogram of CWTs as background information (especially in the high frequency ranges). This causes difficulties for the detection of continuously excited frequencies (especially those with small modal participation). The MRA-based iterative scheme can reduce the noise-effects; however, the deblurring effects can still be considerable in the enhanced data. Hence, the concepts of XWT and the autocorrelation of CWT coefficients are used as an additional step to reduce noise-effects. These effects, however, still remain in both the XWT and autocorrelation analysis. In this regard, in this study, the energies of wavelet-based results are presented for the range $|Z|^2 \in [0.02,1] \times \mathrm{Max}|Z|^2$, to eliminate noise-effects.

In brief, to achieve more reliable results, it can be recommended to use independently different denoising-detecting approaches. And then the results are compared with each other, e.g., those from the wavelet, HHT and Fourier transforms [62,63].

Abovementioned identifications can also be classified as the output-only modal identification, since modal parameters are only determined by the output (recorded) data (caused by wind with stochastic feature) [64].

At the last stage, the detected frequencies are compared with those of a linear undamaged finite element (FE) model. Most of the time, these two types of frequencies may not be the same and FE models cannot precisely predict modal frequencies even for undamaged structures

[65]. The main reasons are: 1) conservation in designs; 2) improper considering of the torsional eccentricity; 3) foundation compliance effects [65]; 4) the effects of damaged parts and flaws (for damaged systems).

In brief, there are other methods for MRA-based studying, such as: 1) the Hilbert-Huang transform (HHT) [38,66] and the modified HHT method [67–70] (both developed for nonlinear signals); 2) the synchrosqueezing transform [71–73] and its generalizations [74,75].

Finally, it should be mentioned that the aforementioned signal enhancement technique with the iterative denoising method can be integrated (as a pre-processor) with other wavelet-based methods developed for the modal parameter identification, see Refs. [13,19,76].

After the signal processing stage, it is necessary to detect damages in the structure by the direct or inverse approaches to consider flaw or damage effects and then in the next step to consider them in simulations. Flaw detections are complex due to the fact that the proper solution of these inverse problems are challenging because of their inherent uncertainty, both in their spatial locations and material properties due to fracture and softening [77]. This uncertainty leads to developing different detection algorithms [78], stochastic modeling [79] and sensitivity/uncertainty analysis [80,81]. Forward simulations of cracks and flaws leads to major challenges to adjust the interfaces to the discretization, which requires efficient remeshing [82–84], division [85], and adaptation [86,87] techniques. An efficient alternative approach is the extended finite element method (XFEM) [15,16] or modifications of it such as the smoothed XFEM [17,18], the phantom node method [88], certain multi-scale methods for fracture [89–92], or phase-field problems [93,94]. Though XFEM has mostly applied to fracture problems, there are also several applications of XFEM related to this topic, i.e., inverse analysis and optimization [32–38]. Similar advantages are observed in peridynamics and dual-horizon peridynamics [95,96], meshfree methods [97–99], partition of unity [100], cracking particles methods [101–103], or extended meshfree methods [104]. Another powerful tool to accurately capture complex geometries accurately is the isogeometric analysis (IGA) [105–108], applied to numerous problems including thin shells [109–112], or optimization [113]. Furthermore, IGA can also be used in an adaptive analysis [79–81]. There are also contributions of combining the advantages of XFEM and IGA [110,114].

This work is composed of seven parts. Section 2 explains the general features of the periling tower and the corresponding ambient vibration tests. Section 3 reviews different one-step denoising techniques by discrete wavelets. There, some common wavelet-based denoising approaches and corresponding effective parameters are also presented. Section 4 devotes to issues related to the iterative denoising and a simple criterion for the adaptive threshold selection. Section 5 surveys three wavelet-based signal processing and pattern recognition tools: XWT, spectral powers and autocorrelation analysis of WTs. Section 6 presents the signal enhancement and frequency detection of the recorded data from the ambient vibration test. The concluding remarks are presented in Section 7.

2 Ambient test on the Ammonium Nitrate periling tower

The petrochemical complex, constructed in 1959, is placed 45 Kilometres north of the city of Shiraz, Iran. The Ammonium Nitrate periling unites composed of two reinforced concrete towers, including the process tower and the elevator tower. The process tower is a cylindrical podium overtopped with a rectangular structure. Four steel chimneys with the height of 25 m diameter of 1.9 m and thickness of 0.5 cm are attached to the top of cylindrical part of the process tower between the heights of 55.7 and 80.7 m (Fig. 1). A schematic illustration of the tower and the corresponding cross-section are presented in Fig. 2. The towers are attached to each other at the heights of 47.7, 50.6, and 55.7 m.

Considering degradation and deterioration from its original condition and increasing vibrational response (mainly due to stiffness reduction), motivated the owners to pursue safety evaluations and potential rehabilitation approaches. Figure 3 depicts some deteriorated parts of the structure of the process tower. The initial assessment of both towers revealed that:

1) Although, during visual tests many parts of reinforced concrete structures seem undamaged, but random petrographic test results provide owners with critical deterioration of cement gel, which extends up to 75 mm inside the outer surfaces.

2) Because of operational conditions and serious health consequences, it is somehow impossible to have access to many parts of process tower's inner surface.

3) Considering the explosion-sensitivity of products.

First, the specifications of instruments and their installation details should be determined to obtain reasonable results. These specifications depend on the dynamic properties of structure, the dynamic characteristics of operational systems and specifications of environmental excitation. The frequency range of some operating machineries is from 30 up to 1500 RPM. The machineries include (but not limited to) stacks, hovers, compressors, condensers and elevator. These machineries could not be turned off during the ambient test, according to the owner's operational protocols.

Regarding accelerometers, a variable capacitance is selected with nominal sensitivity threshold of 1 V/g for the pre-test phase. Observations in the pre-test phase show that *SNR*s are extremely low; this means more sensitive accelerometers are needed for the main test. Hence, the Kinematics' force balance accelerometer (FBA11) is

Fig. 1 Ammonium Nitrate periling tower.

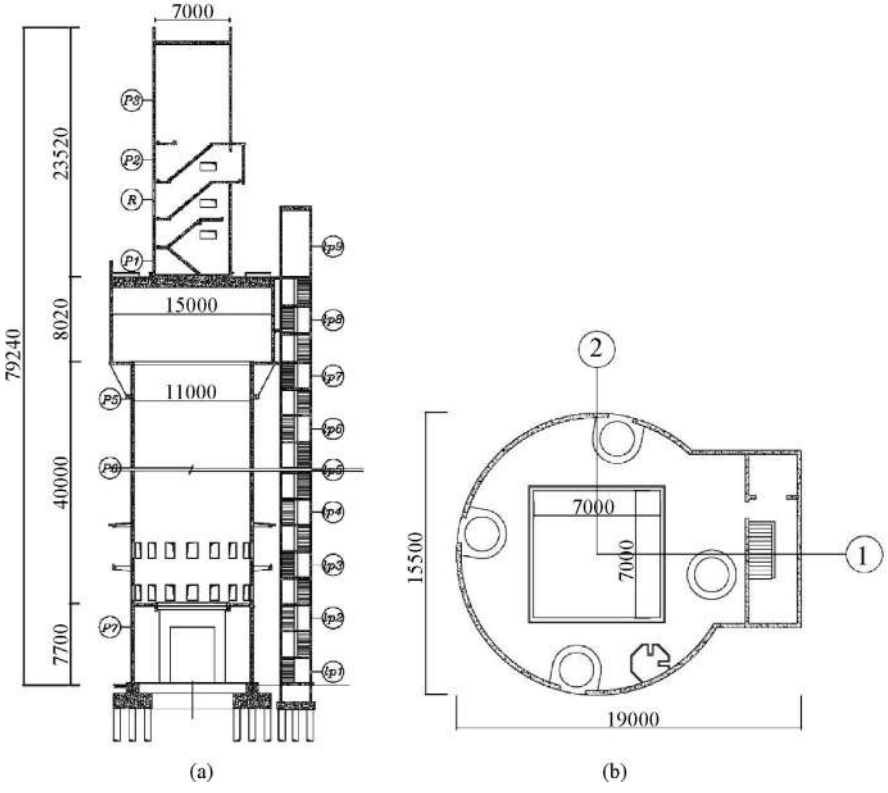

Fig. 2 Recording locations and directions: (a) locations of data recording; (b) recording directions "1" and "2" (unit: mm).

nominated for the main test. This accelerometer has 100 Hz band-width, adjustable sensitivity ranging from + 5 up to + 80 V/g and a dynamic domain equivalent to 140 dB. Also, digital data loggers with ten-simultaneous channels of 24 bit resolution and effective band-width of 50 KHz are used to restore vibrational data.

Another crucial question is about "height-wise and/or plan-wise arrangements of the loggers" during the data accumulation phase. It is extremely preferable to install sensors at antinode locations to catch maximum

Fig. 3 Some examples of concrete destruction.

amplitudes of the structure; however, other factors such as location accessibility, safety considerations and existing vibrational aliasing adjacent to heavy machineries put great limitations on locations of the sensors.

Spatial locations of sensors along the tower and recording directions "1" and "2" are illustrated in Fig. 2. Acceleration recorders on the tower are denoted by P_i where $i \in \{1,...,7\}$, and the recorder R is the reference one. Recording directions for the recorded data at the main tower are denoted by k as P_{ik} for $k \in \{1,2\}$. The ambient vibration test is performed by the wind load and the corresponding responses are recorded by the sampling step $\Delta t = 1/100$ s. Due to the limitation of sensors, signals are recorded in different times.

3 MRA-based denoising and enhancement of data

3.1 Denoising by discrete wavelets

In this subsection, wavelet-based denoising methods and their effective parameters are studied [46].

3.1.1 MRA-based denoising

In general, wavelet-based denoising can be summarized as: 1) estimation of noise level in a process; 2) modification of detail (wavelet) coefficients $\{d(j,k)\}$ (measuring local fluctuations), where the modified set is denoted by $\{\hat{d}(j,k)\}$; 3) reconstruction of the denoised signal by both $\{\hat{d}(j,k)\}$ and unchanged scale coefficients $c(J_{\min},l)$ (reflecting overall smooth variations) [46,47], where $j \in \{J_{\min},J_{\min}+1,...,J_{\max}\}$ denotes the resolution level, where in $J_{\min}$ ($J_{\max}$) shows the coarsest (the finest) resolution level with the sampling step $1/2^{J_{\min}}(1/2^{J_{\max}})$; k denotes the location of the wavelet functions in the spatial domain, as $(2k+1)/2^{j+1} \in [0,1]$; and l denotes the location of the scaling functions in the spatial domain, as $l/2^j \in [0,1]$ [46].

The modifying stage can be performed by the thresholding technique. For instance, for a pre-defined threshold ε, detail coefficients below this threshold are set to zero. This simple kill-or-keep method is known as the hard thresholding [46–48]. To prevent sudden jump in modified (thresholded) detail coefficients, there is another simple and famous approach known as the soft thresholding method, defined as [46–48]:

$$\hat{d}(j,k) = \begin{cases} 0, & |d(j,k)| \leqslant \varepsilon, \\ \mathrm{Sign}[d(j,k)][d(j,k) - \varepsilon], & |d(j,k)| > \varepsilon. \end{cases} \quad (1)$$

The threshold value can be independent or dependent to the resolution level j. The level independent one is known as the global thresholding, where a single threshold is used for all resolutions. For the level dependent case, a threshold value ε_j is used for the level [48].

Regarding the number of iterations for denoising (thresholding), two different approaches have been developed:

1) the one step [44–49];

2) the iterative method, also known as the peeling scheme [51–57].

In the first approach, the noise is cleaned by the one step of thresholding (with either a global or level-dependent one), while in the iterative method, the noise is removed layer by layer (by repeating a denoising procedure on the denoised signal resulted from the previous step) until a convergence criterion is satisfied [51–57]. In general, for estimation of the threshold values, two general approaches exist: theoretical [46,48], and empirical [58].

For the theoretical case, some famous approaches are: *Universal*, *SURE*, and *GCV* (Generalize Cross Validation) [46–48]. They all try to minimize the mean squared error,

$MSE(\varepsilon)$. These three methods are available for both global and level-dependent thresholding methods (see Appendix A for more information). In the empirical approach, the threshold is determined by a criterion, e.g., the curve of *SNR* against ε (threshold). In this case, the proper threshold value is the one maximizing *SNR*.

To quantify the performance of different denoising methods and wavelet family effects, two criteria are considered based on the *MSE* concept: *SNR* and *PSNR* [47,48]:

$$SNR = 10\mathrm{Log}_{10}\left[\frac{\sigma^2(\hat{s})}{\sigma^2(s-\hat{s})}\right],$$

$$PSNR = 10\mathrm{Log}_{10}\left[\frac{\max(|\hat{s}_i|)^2}{\sigma^2(s-\hat{s})}\right], \quad (2)$$

where s and $\hat{s}$ denote the original (noisy) and denoised signals, respectively; $\sigma^2(Z)$ is the variance of Z; $\hat{s}_i$ is the ith element of $\hat{s}$; and $\sigma^2(s-\hat{s})$ measures the variance of the noise: $s-\hat{s}$. Function $R=\sigma^2(s-\hat{s})$ denotes the risk-function, which is equivalent to *MSE* [48]. Both *SNR* and *PSNR* are measured in dB.

The *SNR* and *PSNR* of large values provide better denoised (or compressed) results, because they have inverse proportionality to the variance of noise ($\sigma^2(s-\hat{s})$). For *PSNR*, values larger than 30 dB are sufficient in practical applications [115].

3.1.2 Effective parameters on wavelet-based denoising

To achieve the best denoised signal, especially for the one-step denoising methods, it is essential to select the best denoising method, the best wavelet family and a proper decomposition level. Wavelet functions may be data dependent and this can have significant effects on the denoising performance. For an optimal wavelet, several features should be considered: 1) orthogonality (or bi-orthogonality); 2) support length which may be equivalent to filter length; 3) vanishing order of moments (the jth moment is: $M_j(\psi)=\int x^j\psi(x)\mathrm{d}x$, where $\psi(x)$ denotes the wavelet (detail) function); 4) symmetry. The third condition is also known as the smoothness, approximation, or the regularity condition.

Several wavelet families with different orders are considered in this study: Daubechies (*Db*), *Symlet*, and *BattleLemarie* families [46,49]. For each family, the corresponding wavelet with order N can be represented as: *Db*[*N*], *Symlet*[*N*], and *BattleLemarie*[*N*]. The orthogonal and compact support *Db* and *Symlet* wavelets have, respectively, the most regular and the most symmetric features; while the *BattleLemarie* wavelets are orthogonal and symmetric with infinite support, but the wavelets vanish exponentially.

4 Iterative denoising by discrete wavelets

Wavelet one-step denoising methods are widely used for signal processing problems. However, such approaches may not lead to proper results for data with high-levels of noise (as will be shown in this study). To improve the wavelet-based one-step methods, iterative-based denoising scheme has been developed [51–57]. In this approach, in each iteration, the data having coherent structures in different resolution levels are selected and the remaining information is used as the noise in the next iteration. Due to the high level of noise in the data, the noise is removed from the data as much as possible by decomposing signals to coherent structures and incoherent noise by localizing both in time and frequency domains, simultaneously.

4.1 An algorithm for the MRA-based iterative denoising

In this subsection, the iterative denoising approach proposed in [53–55] is followed. For a noisy signal $\boldsymbol{Z}=\{z[1],...,z[N]\}$, at the first step of the iterative denoising algorithm, it is assumed that the signal $\boldsymbol{Z}$ is totally noise. Then, the coherence and significant features in the noise are gathered.

Detection is performed by decomposing $\boldsymbol{Z}$ by MRA, and then in each resolution level, those detail coefficients ($d(j,k)$), that represent significant phenomena, are detected. In a statistical approach, the distribution of $d(j,k)$ is measured at each scale j and is shown by the variance of the detail coefficients, i.e., $(\sigma^j)^2$. Then, detail coefficients larger than $C\times\sigma^j$ are assumed to belong to a physical phenomenon, where $C=C_n^j$ is a positive constant and $C\geqslant 1$ (n denotes the iteration number). The selected detail coefficients along with the scale coefficients are reconstructed as the first estimation of the denoised signal, and the remaining detail coefficients are reconstructed and named as the updated noise. The above peeling procedure is repeated for the updated noise. At the end of each iteration, the estimated denoised signal is added to the previous one (obtained from the previous step). In brief, the iterative algorithm can be summarized as:

1) For the first iteration, $n=1$, the denoised signal is assumed to be zero: $\boldsymbol{Z}_n=\{z_n[1],...,z_n[N]\}=\{0,...,0\}$, and the noise is $\Delta\boldsymbol{Z}_{n=1}=\boldsymbol{Z}=\{z_n[1],...,z_n[N]\}$.

2) Decompose the noisy signal $\Delta\boldsymbol{Z}_n$ by the DWT to obtain scale coefficients $\{c(J_{\min},l)\}$ and detail coefficients in different resolutions as $\{\{d(j,k)\};\ j=J_{\min},...,J_{\max}-1\}$, where $J_{\min}$ and $J_{\max}$ denote the resolution level of the coarsest and finest resolutions, respectively.

3) Compute the variance of $\{d(j,k)\}$ for each resolution level j as $(\sigma_n^j)^2=\frac{1}{N_j}\|d(j,k)\|_2^2$, where $\|d(j,k)\|_2^2=\sum_k|d(j,k)|^2$, n denotes the iteration number; and N_j is the length of vector $\{d(j,k)\}$ (notice that:

$\mu = \sum_k d(j,k) = 0$).

4) For each resolution level j, compute the threshold as $T_n^j = f(\sigma_n^j)$. It is assumed: $f(\sigma_n^j) = C_n^j \sigma_n^j$, where $C_n^j \geqslant 1$ is a constant.

5) Detect the noise coefficients by the hard thresholding method. Coefficients $d(j,k)$ can be decomposed as: $d(j,k) = \hat{d}(j,k) + \Delta d(j,k)$, where $\hat{d}(j,k) \geqslant T_n^j$ and $\Delta d(j,k)$ denotes the noise coefficients with values less than T_n^j.

6) Reconstruct the modified detail coefficients $\{\hat{d}(j,k);\ j = J_{\min},...,J_{\max}-1\}$ with $\{c(J_{\min},l)\}$ (from the second step). The reconstructed signal is $\hat{\boldsymbol{Z}}_n = \{\hat{Z}_n[1],...,\hat{Z}_n[N]\}$.

7) Reconstruct the detail coefficients belonging to noise, i.e., $\{\{\Delta d(j,k)\};\ j = J_{\min},...,J_{\max}-1\}$ with zero approximation coefficients, $\overline{c}(J_{\min},l) = \{0,...,0\}$. The reconstructed signal is $\Delta \boldsymbol{Z}_{n+1} = \{\Delta Z_{n+1}[1],...\Delta Z_{n+1}[N]\}$.

8) Update the estimated (denoised) signal as: $\boldsymbol{Z}_{n+1} = \{z_{n+1}[1],...,z_{n+1}[N]\} = \{z_n[1],...,z_n[N]\} + \{\hat{z}_n[1],...,\hat{z}_n[N]\}$.

9) Update the noisy signal to be $\Delta \boldsymbol{Z}_{n+1}$, and go back to the second step (to restart a new peeling procedure).

10) This iteration is terminated after a predefined loop-number or reaching a termination criterion, $|STC_{n+1}| < \varepsilon$ where $STC_{n+1} = \|\Delta \boldsymbol{Z}_n\|_2^2 - \|\Delta \boldsymbol{Z}_{n+1}\|_2^2$ and ε denotes a positive constant.

4.2 A simple criterion for choosing C_n^j

The heart of the iterative denoising method is the proper selection of the variance-dependent thresholds controlled by the coefficients C_n^j. While some constant values of C_n^j were empirically proposed for different applications (e.g., $C_n^j = 3$ or $C_n^j = 2.5$) [53], few computational approaches were proposed based on extra information about data, such as their experimental distributions [55,56]. One drawback of the constant C_n^j values (in Refs. [53,116]) is that they can vary for different signals recorded even in one study. In this regard, a flexible approach is needed for adaptive selection of C_n^j values.

In this study, a simple method is proposed based on measuring the *PSNR* and *SNR* values for several C_n^j values. Admissible values C_n^j for correspond to cases where $PSNR \geqslant PSNR^*$; here, it is assumed that $PSNR^* = 30$ [115]. The largest acceptable C_n^j can be used as the first estimation of C_n^j in the iterative denoising method. The present study shows that this selection can be affected by other important parameters:

1) The continuity feature of denoised signals to prevent unphysical gaps in denoised data.

2) Sufficiently large values of *SNR*s.

The selection procedure for C_n^j is explained in detail in Section 6 for different recorded data.

5 Signal processing of the enhanced data by continuous wavelet transforms (CWTs)

After the signal-enhancement stage, the signal processing step is performed by CWTs for detection of time-frequency information in the data.

In this study, the complex Morlet wavelet is used for detection of instantaneous frequencies and pattern recognitions. Parameters of the Morlet wavelet are: $\upsilon_b = 2$ (is the bandwidth frequency) and $\upsilon_c = 1.10$ (denotes the central frequency). Hence, the inequality condition $\sqrt{\upsilon_b}\upsilon_c \geqslant \sqrt{2}$ is satisfied for this wavelet family (defined as $\psi(t) = \frac{1}{\sqrt{\pi \times \upsilon_b}} e^{2\pi i \upsilon_c t \times e^{-t^2/\upsilon_b}}$). For other possible values of υ_b and υ_c, some other approaches are reviewed in Appendix B.

Based on the CWTs, some effective signal processing tools are: XWT, the autocorrelation of wavelet coefficients and the spectral power. Initially, the concept of the spectral power of WT is reviewed. This helps to identify energy concentrations in the frequency (or scale) domain. The spectral power is defined as:

$$P_W(a) = \frac{1}{T}\int_{t_0}^{t_0+T} |W_\psi f(a,b)|^2 \mathrm{d}b, \tag{3}$$

where a denotes the scaling (dilation) number controlling the width (support) of wavelet functions; b represents the spatial position of the scaled wavelets $\psi(t/a)$; T denotes the duration of data; and $W_\psi f(a,b)$ denotes the CWT of data $f(t)$, defined as $W_\psi f(a,b) = \frac{1}{\sqrt{|a|}} \int_{-\infty}^{+\infty} f(t)\ \psi^*\left(\frac{t-b}{a}\right)\mathrm{d}t$, where the symbol "*" shows the imaginary conjugate of a function.

5.1 XWTs, corresponding spectral powers and autocorrelation of wavelet coefficients

Based on the coefficients of WTs, different analyses can be performed. Three of them are:

1) XWTs: In practical computations, it is often useful to capture possible links between two existing processes (signals). For assessing energy coherencies, the concept of the XWT (denoted by XW_ψ) is introduced. For signals $f(t)$ and $g(t)$, $XW_\psi(f,g)$ is defined as [45]:

$$XW_\psi(f,g) = W_\psi f(a,b) \times W_\psi g(a,b)^*, \tag{4}$$

where symbol "*" shows the imaginary conjugate of a function. The XWT detects zones in the time-frequency space where the two data show the coherency of the power (energy). Since the noise has a random feature, the two recorded data are expected to have uncorrelated energies of

noise in different resolutions and times.

2) Spectral power of XWTs: To detect energy coherencies between two data in the frequency domain, the power of XWTs can also be defined, as:

$$P_{XW}(a) = \frac{1}{T}\int_{t_0}^{t_0+T} |XW_{\psi}(f,g)|\mathrm{d}b. \quad (5)$$

Simultaneous study of XWTs and the corresponding spectral powers helps to identify physical (real) phenomena in data. The energy of WT reveals the continuous distribution/pattern of energies in the time-frequency representation, and at the same time the corresponding spectral power shows the concentration of energies in the frequency domain.

3) Autocorrelation of WTs: This operator measures the correlation of a signal with a shifted copy of itself. It assists similarities or repeating patterns in the signal as a function of time delay or time lag. One example of such feature is the detection of periodic signals covered with noise. For the signal $\{x_i\}$, where $i = 1,...,n$, the autocorrelation $R(\tau)$ is defined as:

$$R(\tau) = \frac{\sum_{i=1}^{n-\tau}(x_i-\hat{\mu})(x_{i+\tau}-\hat{\mu})}{\sum_{i=1}^{n-\tau}(x_i-\hat{\mu})^2}, \quad (6)$$

where $\hat{\mu} = (\sum_{i=1}^{n} x_i)/n$ denotes the mean value of the signal $\{x_i\}$, and τ is the time lag.

To integrate the MRA with the autocorrelation concept, at the scale a, the autocorrelation of $W_{\psi}f(a,b)$ is evaluated over the translation parameter b. This procedure is repeated for different a values. For each scale, this helps capturing similarity features through time, or detecting the repeating patterns of data. This type of detection is nearly free from noise effects, since, stochastic coefficients due to noise do not have correlation with each other. In this study, it is shown that this transform is especially important for capturing weakly excited responses or vibration modes (in ambient tests) which cannot be detected by other transforms. Frequencies for modes with small participations have the wavelet coefficients of small values; hence, these frequencies may not be distinguishable from their wavelet energies, XWTs or their spectral densities.

It should be noted that, the scaling parameter a can be related to the corresponding frequency υ_a (in Hz) based on the central frequency of the scaled- shifted wavelet $\psi_{a,b}(t)$, as:

$$\upsilon_a = \frac{\upsilon_c}{a \times \Delta}, \quad (7)$$

where $\psi_{a,b}(t) = \psi((t-b)/a)/\sqrt{|a|}$, $\Delta = \mathrm{d}t$ denotes the sampling period, and υ_c represents the central frequency of the wavelet function $\psi(t)$ in Hz.

6 Results: the signal enhancements and the frequency detection of the ambient vibration test

The effects of regularization- and wavelet-based denoising schemes are now studied for different data in this section. The recorded data $P21$, $P31$, $P51$, $P12$, and $P72$ are presented in Fig. 4 with the sampling time step $\Delta T = 0.01$. The denoising or enhancing procedure is performed with the MRA and the regularization approaches. For the MRA-based denoising approach, both the one-step method and the iterative scheme are studied. For the regularization-based denoising scheme see Appendix C.

6.1 The one-step denoising approach

6.1.1 Denoising with the regularization approach

Let us consider the signal P12. At the first step, it is essential to estimate a proper value for the regularization parameter p (or λ). This can be performed empirically by the *SNR-p* curve [58]: the proper value that maximizes *SNR*. These curves are presented in Fig. 5 for the constraints $\Omega(f)_{\mathrm{TV}}$, $\Omega(f)_{L^2}$, and $\Omega(f)_{\mathrm{Sobolev}}$. It is obvious that the curves do not have any extrema. Due to the high-level of noise, the *SNR* values can even be negative, and for the large values of p, the *SNR* values increase rapidly. For checking the denoising performance, the residual noise (after the denoising stage) and the corresponding energy in the wavelet space (by the complex Morlet wavelet with parameters $\upsilon_b = 2$ and $\upsilon_c = 1.10$) are presented in Fig. 6 for the constraints $\Omega(f)_{L^2}$ and $\Omega(f)_{\mathrm{Sobolev}}$, where $p = 0.98$. The energies are presented for the range of $0.02\mathrm{Max}[|W_{\psi}|^2] \leqslant |W_{\psi}|^2 \leqslant \mathrm{Max}[|W_{\psi}|^2]$. It is evident that the energies of the noises do not contain localized stochastic information; instead, they contain several instantaneous frequencies excited continuously through time. Such information can be physically justified as the modal frequencies of the structure. Hence, this denoising approach is not efficient.

6.1.2 DWT-based one-step denoising methods

The performance of different one-step DWT-based denoising approaches is studied for signals $P12$ and $P51$. Denoising approaches are mentioned in Table 1; the term "Level" indicates the level depending thresholding.

For the signal $P51$, the corresponding results based on *Symlet*[12] wavelet with $N_d = 13$ (the number of decomposition levels) are presented in Fig. 7. For $P12$ and $P51$, the performance of different denoising methods, measured by the *SNR* and *PSNR* criteria, is also presented in Table 2.

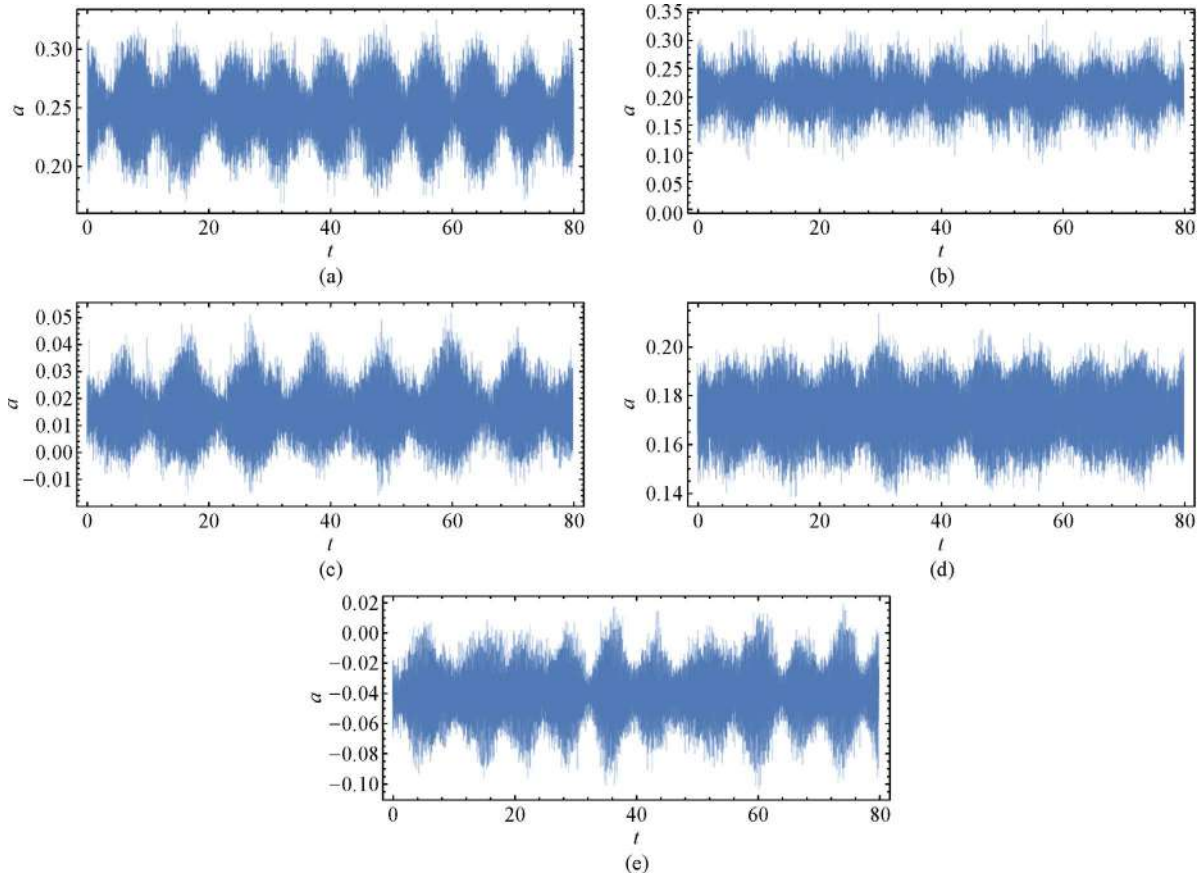

Fig. 4 Recorded accelerations at different stations: (a) signal *P*21; (b) signal *P*31; (c) signal *P*51; (d) signal *P*12; (e) signal *P*72.

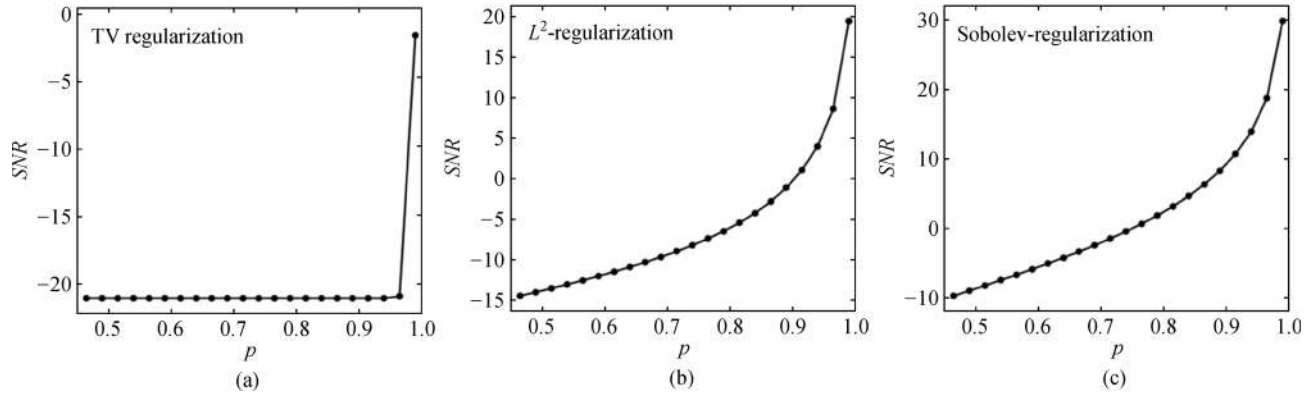

Fig. 5 Empirical evaluation of p values based on *SNR*-p curves for data *P*12. (a) *SNR*-p curve by the TV regularization; (b) *SNR*-p curve by the L^2 regularization; (c) *SNR*-p curve by the Sobolev regularization.

This table and Fig. 7 offer that the GCV denoising method leads to the best result for the *Symlet*[12] wavelet with $N_d = 13$. However, in general, this conclusion could not be made. This is studied in terms of different denoising approaches, wavelet families and the number of decomposition levels (N_d) in the following.

The effects of the wavelet family are studied in Tables 3–5 for the GCV method with $N_d = 13$ and the considered wavelet families are: *Db*[*N*], *Symlet*[*N*], and *BattleLemarie* [*N*]. Accordingly, the wavelet-dependency of the results is clear even for the GCV method. The effects of N_d, presented in Table 6, confirm that the values of *SNR* and *PSNR* are in accordance with the values of N_d.

The performance of the empirical approach for the threshold selection is studied in the following. Let us consider the signal *P*12 with both the hard and the soft

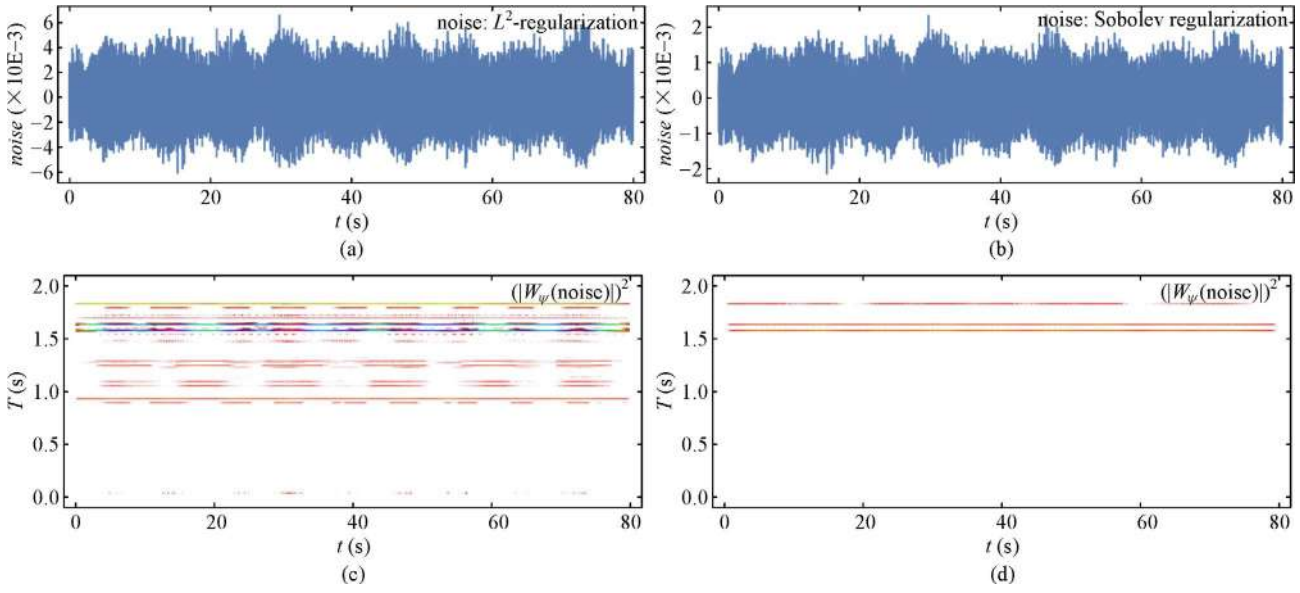

Fig. 6 Residual noise of the regularization-based denoising and corresponding energy in the wavelet space; plotted ranges are $0.02\text{Max}[|W_\psi|^2] \leqslant |W_\psi|^2 \leqslant \text{Max}[|W_\psi|^2]$. (a) The residual noise obtained by the L^2 regularization (by using $\Omega(f)_{L^2}$); (b) the residual noise obtained by the Sobolev regularization (by using $\Omega(f)_{\text{Sobolev}}$); (c) the time-period representation in the wavelet space of the residual noise obtained by $\Omega(f)_{L^2}$; (d) the time-period representation in the wavelet space of the residual noise obtained by $\Omega(f)_{\text{Sobolev}}$.

Table 1 Different denoising approaches with corresponding thresholding method and estimating noise level

denoising method	thresholding approach	estimating method of the noise level
GCV	soft	GCV
GCVLevel	soft	GCV-Level
SURE	hard	SURE
SURELevel	hard	SURE-Level
SUREShrink	soft	SURE
Universal	hard	Universal
UniversalLevel	hard	Universal-Level
VisuShrink	soft	Universal
VisuShrinkLevel	soft	Universal-Level

thresholding approaches. Variations of *SNR* against ε/σ values are presented for different wavelet families in Fig. 8 for $N_{\text{d}} = 13$; where ε and σ denote the threshold and the deviation of a signal, respectively. In Fig. 8, the wavelets are those with the best performance according to Tables 3–5. The results offer that the curves do not have extremum values for *SNR*s; therefore, an empirical threshold cannot be recommended.

6.2 Results for the iterative denoising method

6.2.1 Selection of C_n^j values

For the iterative denoising, the largest possible value of C_n^j for each signal can be estimated by a simple algorithm based on measuring *PSNR* values.

Initially, the effects of C_n^j values on the iterative thresholding is studied for the signal *P*12. Two different values of C_n^j are chosen as $C_n^j = 1.8$ and $C_n^j = 2$. Enhanced signals by thresholds $C_n^j = 1.8$ and $C_n^j = 2$ are presented in Figs. 9 and 10, respectively. The wavelet is *Symlet*[12], with $N_{\text{d}} = 13$ and $N = 10$ (the number of iterations). In these figures, the captured information ($\hat{\boldsymbol{Z}}_n$) and estimated noise ($\Delta\boldsymbol{Z}_n$) are presented at each iteration. In the last row, both the denoised data (i.e., $\boldsymbol{Z}_{1+10} = \sum_{n=1}^{10} \hat{\boldsymbol{Z}}_n$) and the estimated noises (that is: $\boldsymbol{Z} - \sum_{n=1}^{10} \hat{\boldsymbol{Z}}_n$) are presented after ten iterations. The denoised data offer that:

1) For $C_n^j = 1.8$. $SNR = 2.3072$ and $PSNR = 28.145$: an insufficient denoised signal as the *SNR* is small; the denoised signal has several gaps.

2) For $C_n^j = 2$. $SNR = -10.078$ and $PSNR = 24.286$: a false denoised signal; most parts of physical information are eliminated.

Therefore, choosing a proper value for C_n^j is crucial. For this reason, the simple approach, proposed in Section 4.2, is now explained in detail. Variations of the *PSNR* and *SNR* values against C_n^j are illustrated in Fig. 11 for different signals with parameters: *Symlet*[12], $N_{\text{d}} = 13$ and $N = 10$ (the number of iterations). Based on the *PSNR* values and $PSNR^* = 30$, the initially estimated values of C_n^j (the largest possible values) are: 1) For *P*12: $C_n^j = 1.78$; 2) For *P*51: $C_n^j = 1.94$; 3) For *P*31: $C_n^j = 1.95$; 4) For *P*72: $C_n^j = 1.91$; and 5) For *P*21: $C_n^j = 1.96$.

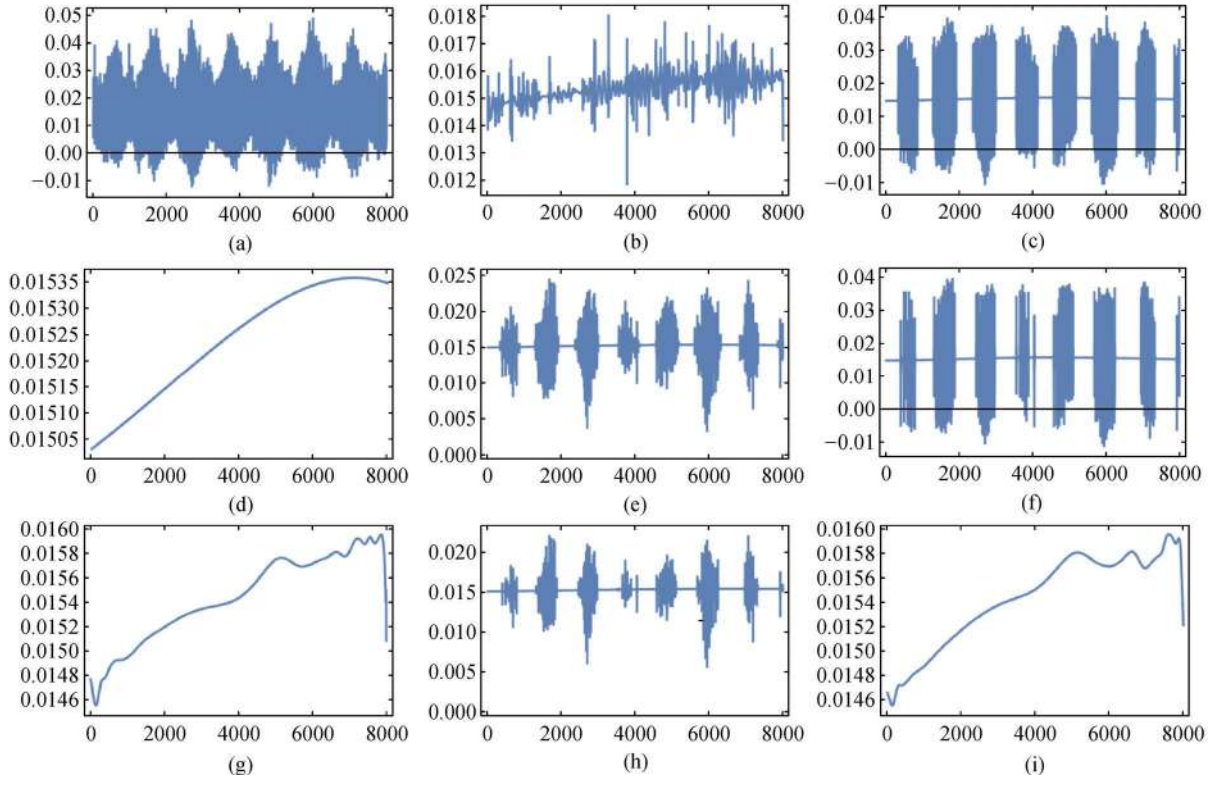

Fig. 7 Denoising of the *P*51 signal with different one-step wavelet-based denoising methods using *Symlet*[12] wavelet where $N_d = 13$. (a) denoising with GCV method; (b) denoising with GCVLevel method; (c) denoising with SURE method; (d) denoising with SURELevel method; (e) denoising with SUREhrink method; (f) denoising with Universal method; (g) denoising with UniversalLevel method; (h) denoising with VisuShrink method; (i) denoising with VisuShrinkLevel method.

Table 2 Effects of denoising with different thresholding methods by the *Symlet*[12] and $N_d = 13$

method	*P*12		*P*51	
	SNR	*PSNR*	*SNR*	*PSNR*
GCV	22.2179	46.72143	18.21671	32.48012
GCVLevel	−33.2626	22.4117	−26.3399	4.871594
SURE	−51.2787	22.2521	−1.3714	14.25517
SURELevel	−51.2787	22.2521	−39.8919	3.420075
SUREShrink	−51.2787	22.2521	−16.3401	8.145114
Universal	−51.2787	22.2521	−4.22646	13.07922
UniversalLevel	−35.1236	22.31927	−29.3122	3.756303
VisuShrink	−51.2787	22.2521	−21.3869	6.866752
VisuShrinkLevel	−45.3760	22.26384	−32.9884	3.602981

In this study, slightly smaller values of C_n^j are used: to prevent developing of artificial gaps, and to have a larger value for *PSNR* in denoised signals, as: 1) For *P*12: $C_n^j = 1.75$; 2) For *P*51: $C_n^j = 1.90$; 3) For *P*31: $C_n^j = 1.90$; 4) For *P*72: $C_n^j = 1.85$; 5) For *P*21: $C_n^j = 1.90$.

For the signal *P*12, with the threshold $C_n^j = 1.75$, the effectiveness of the enhancement (measured by *SNR* and *PSNR*) after each iteration is presented in Table 7. The assumptions are: Two *Symlet* wavelets of orders 4 and 12 with $N_d = 13$ are utilized; at the end of *i*th iteration, for evaluation of *SNR* and *PSNR*, the enhanced results at the *i*th iteration (i.e., $\boldsymbol{Z}_{1+i} = \sum_{n=1}^{i} \hat{\boldsymbol{Z}}_n$) and the initial noisy (raw) data ($\boldsymbol{Z}$) are used. It is evident that even for the *Symlet*[4] the results become sufficiently good after ten

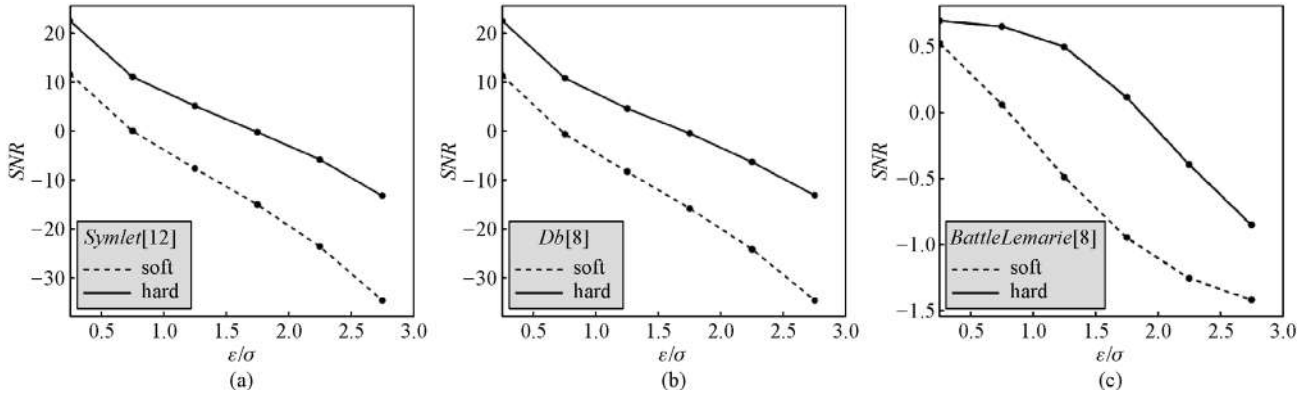

Fig. 8 Variations of *SNR* against ε/σ for P12 signal with different one-step wavelet-based denoising methods, where $N_d = 13$. (a) soft and hard denoising with *Symlet*[12]; (b) soft and hard denoising with *Db*[8]; (c) soft and hard denoising with *BattleLemarie*[8].

Table 3 Effects of denoising with the GCV method for "*Db*" wavelets, where $N_d = 13$

method	*n*(*Db*[*N*])	*P*12		*P*51	
		SNR	*PSNR*	*SNR*	*PSNR*
GCV	2	−44.06220	22.50474	−3.89105	15.11722
GCV	3	−44.60310	22.51398	1.745215	18.18960
GCV	4	16.88966	41.75307	4.907001	20.27852
GCV	5	21.81810	46.31249	10.50614	25.38050
GCV	6	21.80349	46.34828	9.132639	24.06303
GCV	7	21.79715	46.28996	16.05011	30.35188
GCV	8	21.88650	46.39464	19.22092	33.40890
GCV	9	20.92899	45.53208	17.05526	31.40279
GCV	10	−47.54780	22.40617	15.57229	29.81848
GCV	11	−45.98960	22.43916	17.50372	31.65586
GCV	12	−47.04270	22.40797	15.54650	30.10663

Table 4 Effects of denoising with the GCV method for "*Symlet*" wavelets, where $N_d = 13$

method	*n*(*Symlet*[*N*])	*P*12		*P*51	
		SNR	*PSNR*	*SNR*	*PSNR*
GCV	2	−44.06220	22.50474	−3.89105	15.11722
GCV	3	−44.60310	22.51398	1.745215	18.18960
GCV	4	−29.29480	22.63941	1.328582	17.44202
GCV	5	−35.13940	22.37958	6.854628	22.08273
GCV	6	−41.13590	22.55448	16.61225	31.09798
GCV	7	20.87357	45.46648	12.50832	27.23006
GCV	8	−37.22440	22.52614	14.83558	29.36768
GCV	9	−36.51710	22.40699	14.93296	29.30645
GCV	10	−38.40640	22.47555	14.31810	28.91892
GCV	11	16.16067	41.13243	15.13602	29.70963
GCV	12	22.21790	46.72143	18.21671	32.48012

Table 5 Effects of denoising with the GCV method for "*BattleLemarie*" wavelets, where $N_d = 13$

method	*n*(*BattleLemarie*[*N*])	*P*12		*P*51	
		SNR	*PSNR*	*SNR*	*PSNR*
GCV	2	−37.51220	22.48681	14.50130	29.00262
GCV	3	2.524623	28.41792	9.416154	24.65823
GCV	4	−39.45680	22.36815	20.25745	34.51602
GCV	5	−3.82456	21.44457	9.14055	24.06958
GCV	6	−39.71980	22.37107	19.59721	33.88775
GCV	7	−2.11519	20.21495	8.419222	23.10889
GCV	8	−39.93670	22.36848	20.21610	34.49167
GCV	9	−1.67073	19.56586	6.465177	21.24691
GCV	10	−40.13260	22.36773	20.53085	34.79046
GCV	11	−1.32343	19.16377	4.554586	19.54653
GCV	12	−40.3243	22.36709	19.7327	34.01635

Table 6 Effect of decomposition levels (N_d) with *Symlet*[12] wavelet

method	N_d	*P*12		*P*51	
		SNR	*PSNR*	*SNR*	*PSNR*
GCV	1	−9.97622	23.26845	5.658332	19.27875
GCV	2	−19.0964	22.53899	−0.27328	16.60651
GCV	3	−20.6277	22.53432	12.68916	27.32417
GCV	4	−28.2157	22.42929	12.34322	26.96229
GCV	5	−31.7853	22.41064	12.2635	26.88179
GCV	6	17.47486	42.28752	12.57217	27.09593
GCV	7	22.22651	46.72911	12.61731	27.15701
GCV	8	22.22536	46.72797	16.6339	30.97174
GCV	9	22.22257	46.72528	16.63093	30.96646
GCV	10	22.22027	46.72262	18.22178	32.48961

iterations, while with this wavelet the results obtained from the one-step denoising approach are not acceptable (see Table 4).

For the signal P12, both the captured information ($\hat{\boldsymbol{Z}}_n$) and the estimated noise ($\Delta\boldsymbol{Z}_n$) are presented in Fig. 12 at each iteration (or the peeling step), where $C_n^j = 1.75$ and $N_d = 13$. In this figure, the last row includes: the left column: the denoised signal after ten iterations, (i.e., $\boldsymbol{Z}_{1+10}$), and the right column: the estimated noise ($\boldsymbol{Z} = \sum_{n=1}^{10} \hat{\boldsymbol{Z}}_n$).

6.2.2 The feature of the estimated noise by MRA

The effects of the iterative enhancement for different signals are discussed in more detail in this subsection. The energy densities of the final noises, obtained after ten iterations ($\boldsymbol{Z} = \sum_{n=1}^{10} \hat{\boldsymbol{Z}}_n$; see Fig. 10), are presented in Fig. 13 for different signals in the time-frequency representations (obtained by CWT). All computations are performed by the complex Morlet wavelet, where $\upsilon_b = 2$ and $\upsilon_c = 1.10$. The plotted range for the energies is $0.02\text{Max}[|W_\psi|^2] \leqslant |W_\psi|^2 \leqslant \text{Max}[|W_\psi|^2]$. The results confirm that the noises contain localized random-wise information at different times and resolution levels, especially at the high frequency ranges (as expected for noise). For short periods, i.e., $T < 0.5$, stochastic localized information exists and for the range of $0.9 < T < 1.4$, several considerable phenomena occur locally, which may represent the operations of mechanical systems in the tower. These local or stochastic-like data are not important in this study, because only the modal frequencies excited continuously in time are sought.

So far, some mathematical tools have been used to enhance signals. At the next step, it is tried to integrate the physical properties to extract more reliable information

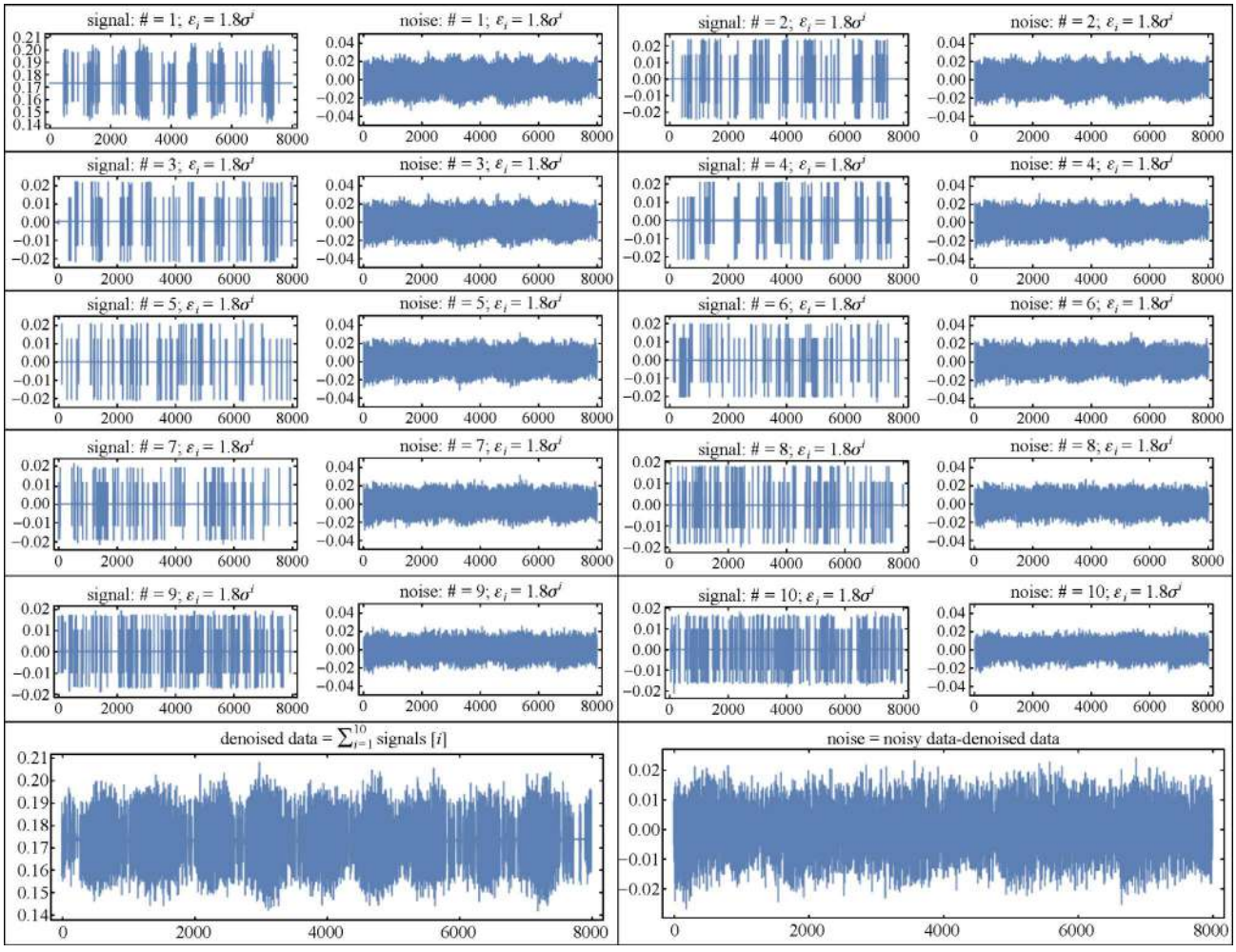

Fig. 9 The iterative thresholding for $P12$ where $C_n^i = 1.8$, *Symlet*[12] and $N_d = 13$. The last row contains final denoised signal and estimated noise.

from the enhanced data. The main idea is that if some information is repeated in different data, they may include the physical responses of the structure. The MRA-based approaches for such detections are XWT and the autocorrelation of wavelet coefficients (since the noise is assumed to have random feature with zero coherence).

6.3 XWTs and autocorrelation of wavelet coefficients for frequency detections

Physical responses are tried to be detected by XWT, the corresponding spectral power and the autocorrelation of wavelet coefficients.

XWT is used for detection of energy coherencies in the enhanced pairs {$P21$, $P31$}, {$P21$, $P51$}, and {$P12$, $P72$}. These signals are enhanced with the iterative algorithm with *Symlet*[12], where $N_d = 13$, and $N = 10$ (the number of iterations). Results presented in Figs. 14, 15, and 16 are for the enhanced pairs {$P21$, $P31$}, {$P21$, $P51$}, and {$P12$, $P72$}, respectively. In each figure, the density of wavelet energies, the corresponding XWT and the spectral powers are provided. In these figures, plotted ranges for $|W_\psi|^2$ and $|W_\psi|$ are $0.02\text{Max}[|W_\psi|^2] \leqslant |W_\psi|^2 \leqslant \text{Max}[|W_\psi|^2]$ and $0.02\text{Max}[|W_\psi|] \leqslant |W_\psi| \leqslant \text{Max}[|W_\psi|]$, respectively.

Based on XWTs and the corresponding powers, the detected frequencies are:

1) Form the pair {$P21$, $P31$} (Figs. 14(e) and 14(f)): 0.88, 0.92, 1.05, 1.09, 1.11, 1.22, 1.24, 1.29, 1.59, 1.64, 1.8, 1.84, 2.12, 2.16, and 2.3 s.

2) Form the pair {$P21$, $P51$} (Figs. 15(c) and 14(d)): 0.88, 0.92, 1.05, 1.09, 1.24, 1.29, 1.59, 1.64, 1.71, 1.78, 1.8, 1.84, 2.12, 2.16, and 2.3 s.

3) Form the pair {$P12$, $P72$} (Figs. 16(e) and 14(f)): 0.88, 0.92, 1.05, 1.09, 1.24, 1.29, 1.55, 1.59, 1.64, 1.8, 1.84, 1.89, 1.96, 2.12, 2.16, and 2.3 s.

Since signals are not recorded simultaneously, periods which are detected in all pairs are assumed to be the possible modal periods. They are: 0.88, 0.92, 1.05, 1.24, 1.29, 1.59, 1.64, 1.8, 1.84, 2.12, 2.16, and 2.3 s. The results also show that due to the semi-symmetric shape of the

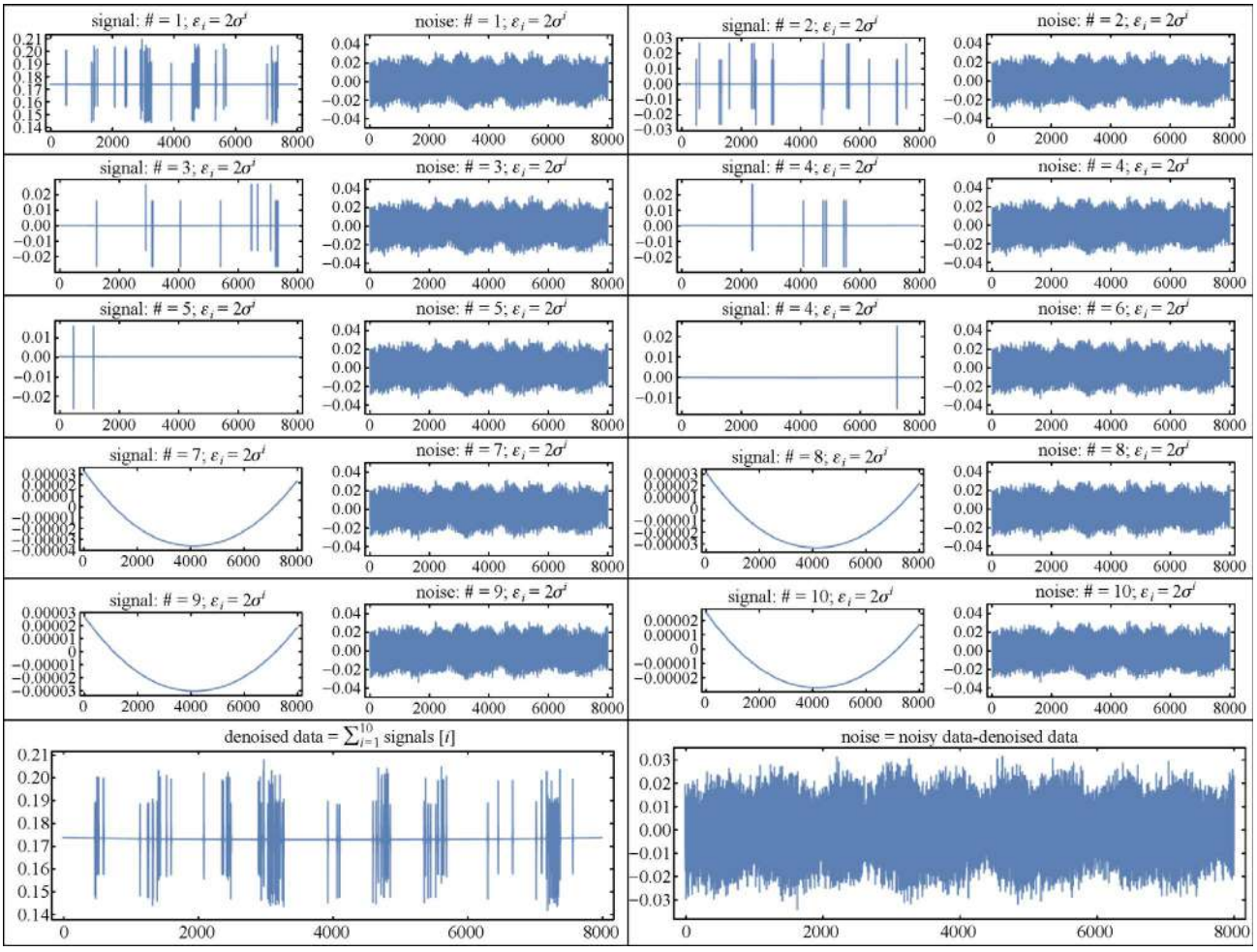

Fig. 10 The iterative thresholding for $P12$ where $C_n^j = 2$, *Symlet*[12] and $N_d = 13$. The last row contains final denoised signal and estimated noise.

structure, there are several pairs of nearly excited periods.

In the following, by the autocorrelation of the wavelet coefficients (of CWTs), interrelationships are studied at different resolution levels of the enhanced data and the results are illustrated in Fig. 17 for $P21$, $P31$, $P51$, $P12$ and $P72$. It is evident that by the autocorrelation transform, it is possible to detect some short periods which are not captured by XWT. The detected short periods are: 0.12 and 0.4 s, which are common in all data. These short periods participate marginally in the ambient vibration test, due to: 1) the nature of wind loading: this type of load mobilizes mainly some first modes; 2) the rigidity of the concrete tower: the participation of higher modes is small for the wind load.

Based on the aforementioned detections, the possible modal periods are mentioned in Table 8. The tower was independently modeled by an undamaged FE model using 3-D continuum elements with linear shape functions [117]. The modal frequencies of the FE model reported in Ref. [117] are presented in Table 8.

Regarding the modal frequencies, the difference between the results may be attributed to: 1) damage existence in different parts of the concrete tower, which is not considered in the FE model; 2) the effects (mass and stiffness) of three operating fans on the top of the main tower, one Hooper and the operation of some mechanical systems in the main tower are not considered in the FE model; 3) the steel-concrete interaction due to the existence of four narrow and long steel towers on the top of the main concrete tower (Fig. 1) and their connection to the concrete tower. In the FE model, steel towers have rigid connections with the main tower, which may not be the case in real structure; 4) ignoring the foundation effects. These differences between theoretical and experimental results were also reported in some independent studies [65].

7 Conclusions

In this study, the main novelty from the application-wise

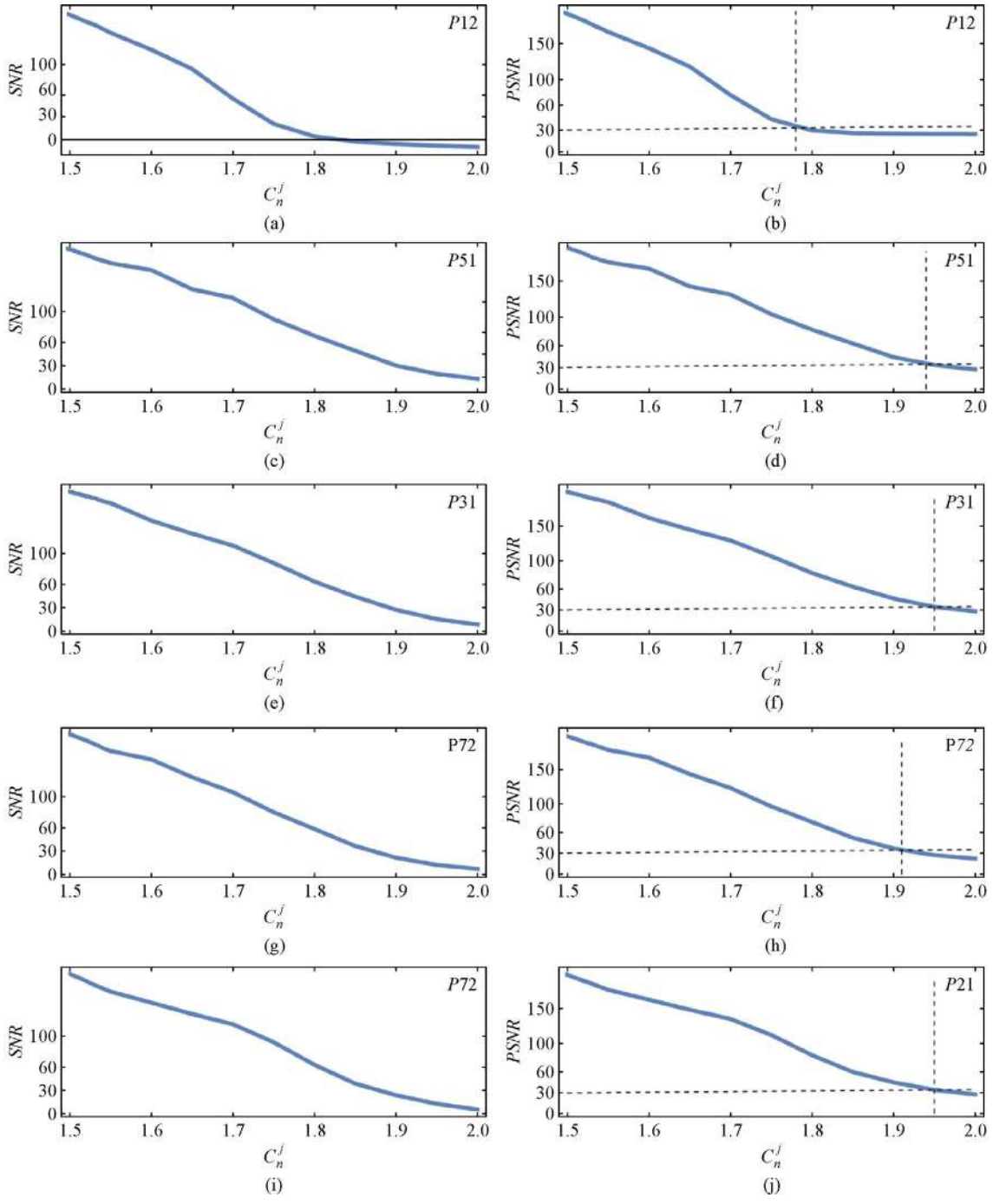

Fig. 11 Determination of thresholds for C_n^j for different enhanced data; *SNR*s and *PSNR*s are obtained by the iterative denoising method by the wavelet *Symlet*[12], $N_d = 13$ and ten iterations. (a) *SNR*-C_n^j for *P*12; (b) *PSNR*-C_n^j for *P*12; (c) *SNR*-C_n^j for *P*51; (d) *PSNR*-C_n^j for *P*51; (e) *SNR*-C_n^j for *P*31; (f) *PSNR*-C_n^j for *P*31; (g) *SNR*-C_n^j for *P*72; (h) *PSNR*-C_n^j for *P*72; (i) *SNR*-C_n^j for *P*21; (j) *PSNR*-C_n^j for *P*21.

point of view is introducing the iterative enhancement approach. For this approach, then, a computational method is suggested to help in choosing proper values of the iterative algorithm.

Initially, two general MRA-based approaches have been examined for the enhancement of high-level noisy signals recorded from the ambient vibration tests: the one-step and the iterative denoising methods. The regularization-based denoiser is also studied as the one-step denoiser. For the data with small values of *SNR*, the results of the variational-based minimization (the regularization) and the MRA-based one-step denoising methods confirm that:

1) Outputs can be incorrect (Figs. 6 and 7).
2) For the variational-based denoising, there is no

Table 7 Iterative denoising of data *P*12 with parameters: $C_n^j = 1.75$ and $N_d = 13$

iteration	*Symlet*[4]		*Symlet*[12]	
	SNR	*PSNR*	*SNR*	*PSNR*
1	−7.55393	24.76396	−7.21248	24.65147
2	−4.92225	25.24466	−4.53529	25.20301
3	−3.10526	25.76809	−2.92566	25.62346
4	−1.62498	26.31642	−1.5398	26.14033
5	−0.1176	26.99467	−0.21442	26.73450
6	1.565725	27.89154	1.296935	27.54208
7	3.492652	29.12365	3.141206	28.69235
8	5.906256	30.92646	5.588525	30.51896
9	9.267875	33.77444	9.015204	33.39050
10	14.43995	38.5877	13.90964	38.10661
11	22.86539	46.97153	20.82031	44.92097

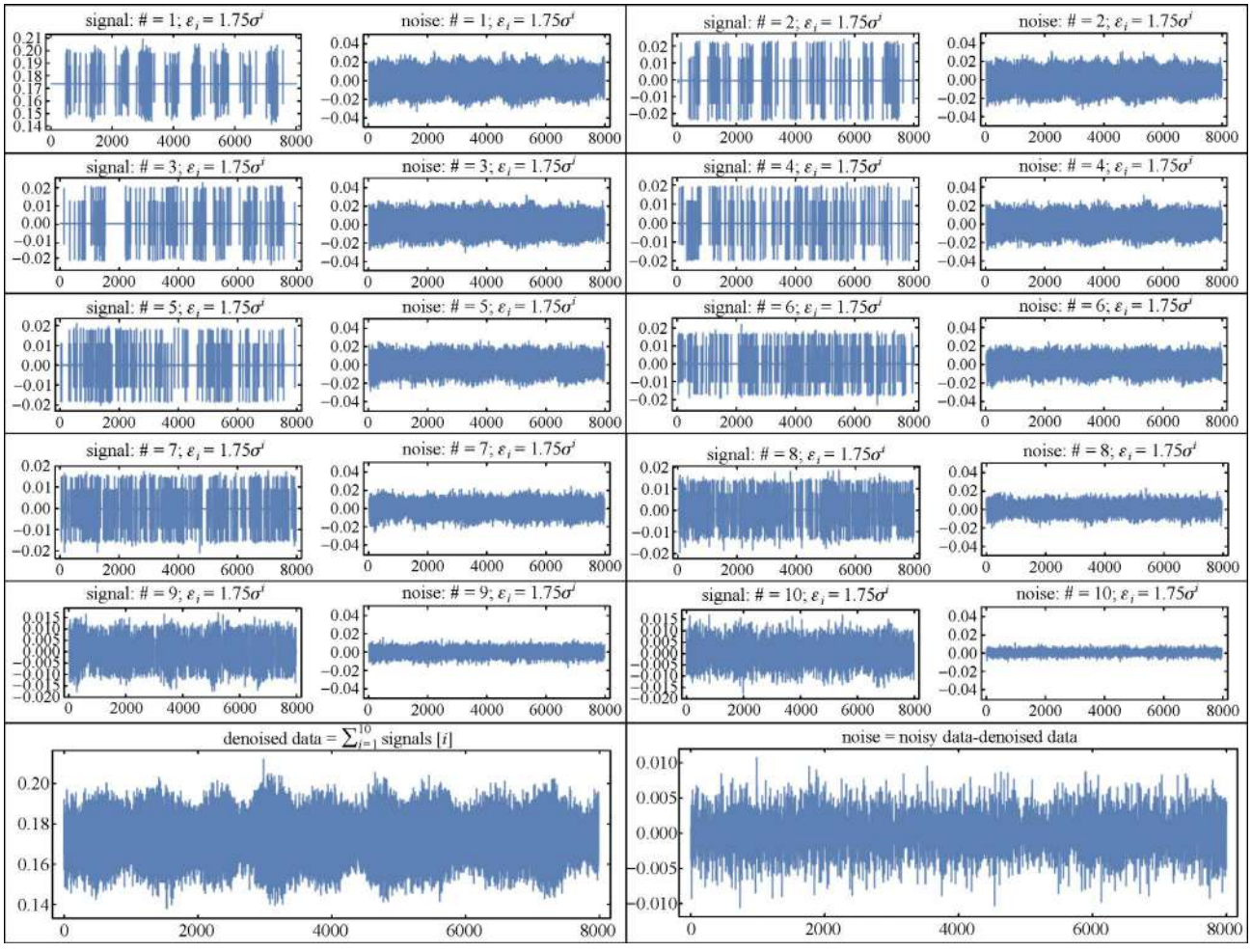

Fig. 12 Iterative denoising of the signal *P*12 with ten iterations; both denoised signal and estimated noise are provided at each iteration (rows 1–5). The last row contains final denoised signal and estimated noise; evaluations are obtained with: *Symlet*[12], $C_n^j = 1.75$ and $N_d = 13$.

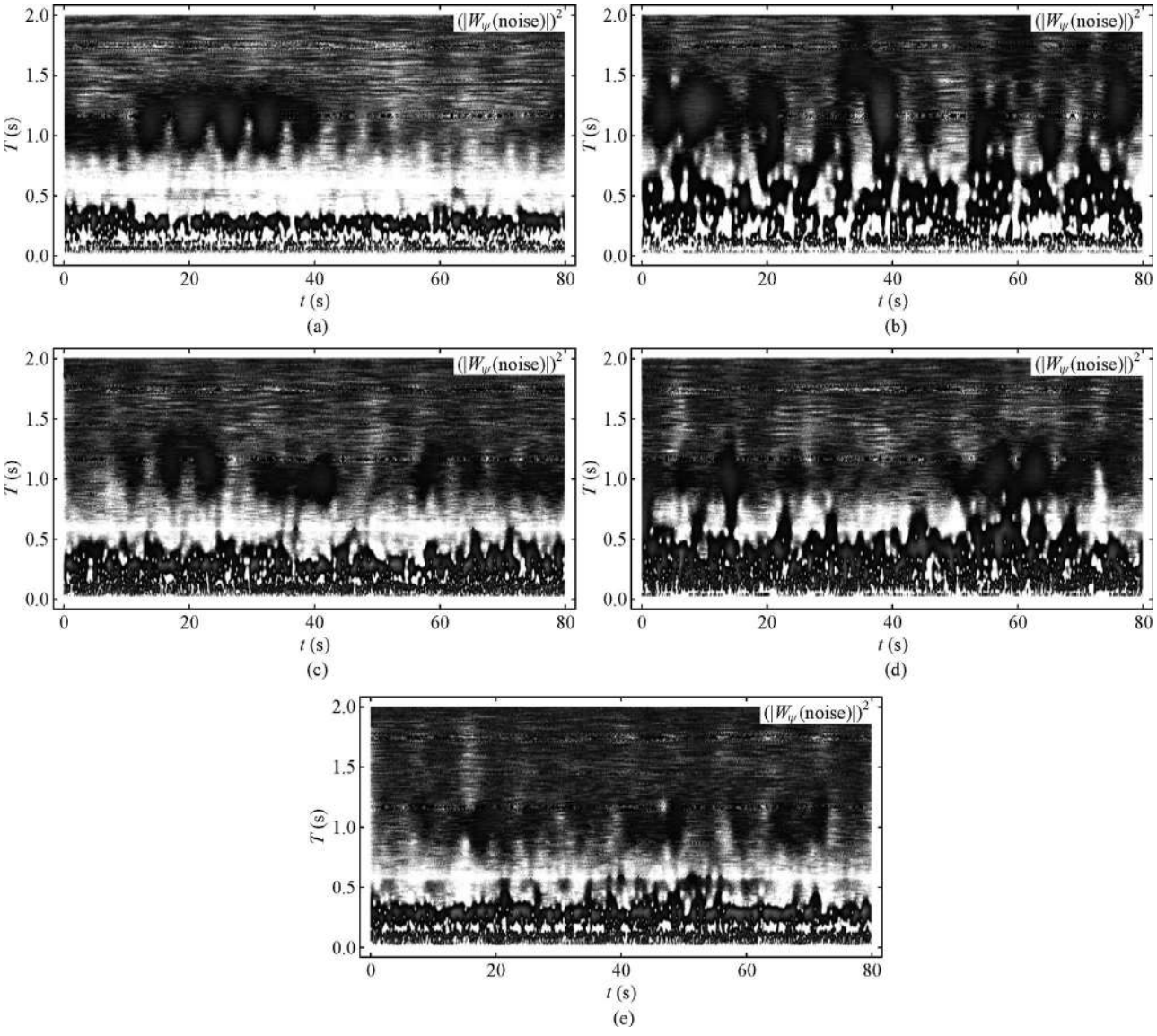

Fig. 13 Energy Density for remaining noise after ten iterations of the peeling algorithm where $N_d = 13$; the energies are evaluated by the complex Morlet wavelet with parameters $\upsilon_b = 2$ and $\upsilon_c = 1.75$. Energies are presented for the range $0.02\text{Max}[|W_\psi|^2] \leqslant |W_\psi|^2 \leqslant \text{Max}[|W_\psi|^2]$. (a) noise of $P12$ in the wavelet space where $C_n^j = 1.75$; (b) noise of $P51$ in the wavelet space where $C_n^j = 1.90$; (c) noise of $P31$ in the wavelet space where $C_n^j = 1.90$; (d) noise of $P72$ in the wavelet space where $C_n^j = 1.85$; (e) noise of $P21$ in the wavelet space where $C_n^j = 1.90$.

optimum value of *SNR* in the empirical approach for estimation of λ (Fig. 5). Moreover, denoised data (even with marginal effects of regularization) may contain physical information (Fig. 6).

3) For wavelets, both empirical and theoretical approaches are unsuccessful for estimation of threshold values (Figs. 7 and 8).

4) Results are very sensitive to wavelet families (Tables 3, 4, and 5).

5) Different thresholding methods lead to different results (Table 2).

6) The number of decomposition levels is also important (Table 6).

For the iterative denoising approach in high-level noisy data, the results offer:

1) Different C_n^j values are needed for different recorded data (Fig. 11); hence, it is essential to use an adaptive approach for selection of C_n^j.

2) It can enhance the signals (see captured noise in Fig. 12 and corresponding stochastic density of energy in Fig. 13).

3) The method can detect some stochastic-like data, which confirms the importance of such enhancements (Fig. 13).

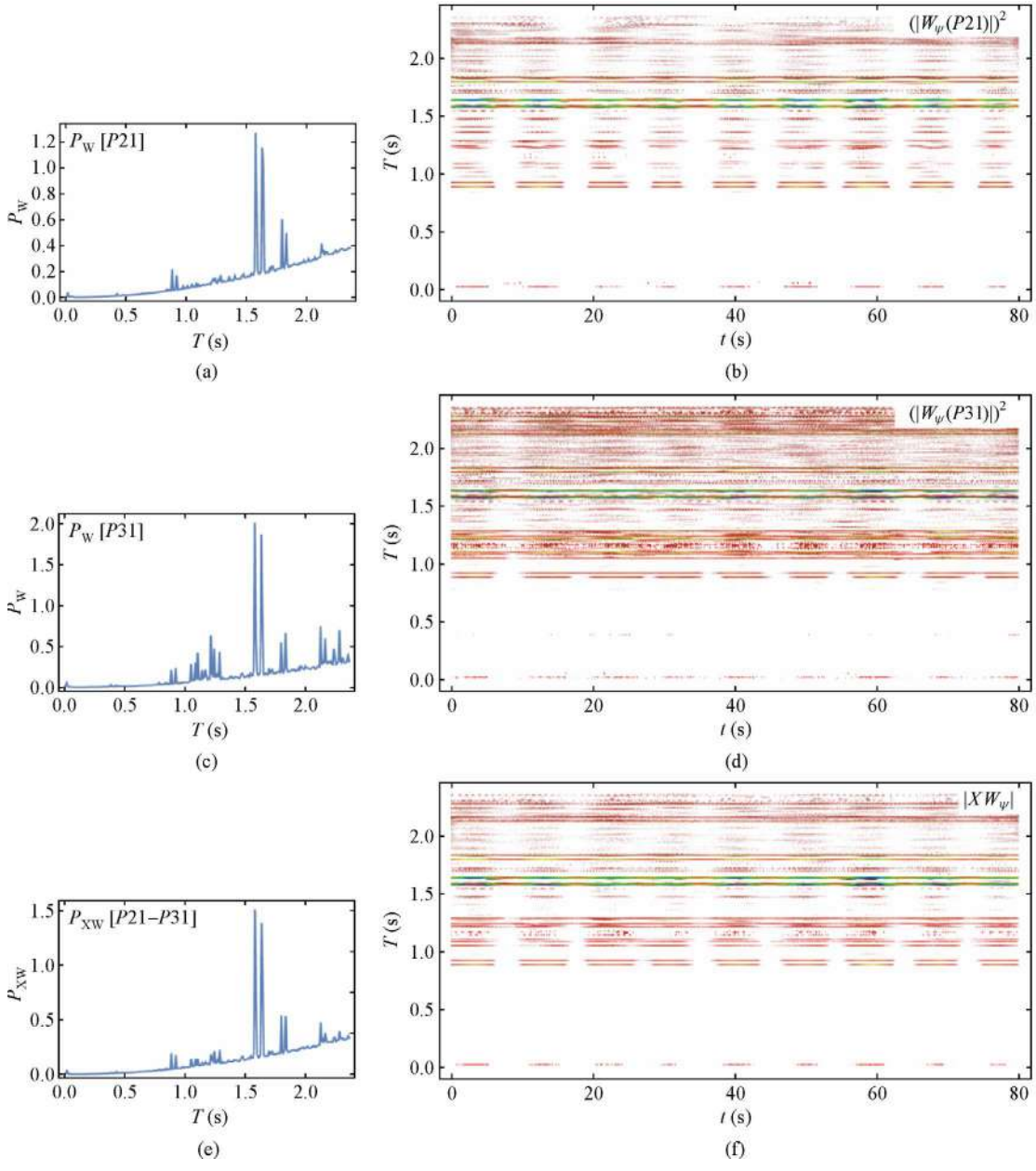

Fig. 14 Powers and energies of WTs of enhanced signals $P21$ and $P31$ and corresponding XWT and spectral power of XWT; plotted ranges are $0.02\text{Max}[|W_\psi|^2] \leqslant |W_\psi|^2 \leqslant \text{Max}[|W_\psi|^2]$ and $0.02\text{Max}[|W_\psi|] \leqslant |W_\psi| \leqslant \text{Max}[|W_\psi|]$. (a) The spectral power of the enhanced data $P21$, evaluated by $|W_\psi(P21)|^2$; (b) the density of energy for the enhanced data $P21$, $|W_\psi(P21)|^2$; (c) the spectral power of the enhanced data $P31$, evaluated by $|W_\psi(P31)|^2$; (d) the density of energy of the enhanced data $P31$, $|W_\psi(P31)|^2$; (e) the spectral power of XWT for the enhanced data $P21$ and $P31$; (f) the density of $|XW_\psi|$ for the enhanced data $P21$ and $P31$.

4) Noise cannot completely be removed (see the localized features in Fig. 15).

5) The results are not so sensitive to the wavelet orders or families (Table 7).

6) While some criteria can be introduced (e.g., Fig. 11) for the threshold estimation, the trial and error method can also be recommended for determination of threshold (this is clear by comparing Figs. 9, 10, and 12).

After the enhancement of the high-level noisy signals (from ambient vibrations) by the iterative algorithm, it has been tried to detect excited frequencies by some MRA-based signal-processing approaches: the cross-wavelet analyses, corresponding spectral powers and the auto-correlations of wavelet coefficients. CWTs have been performed with the complex Morlet wavelets for capturing both instantaneous frequencies and corresponding excitation patterns in the time-frequency representations.

An excited frequency is known as a physical phenom-

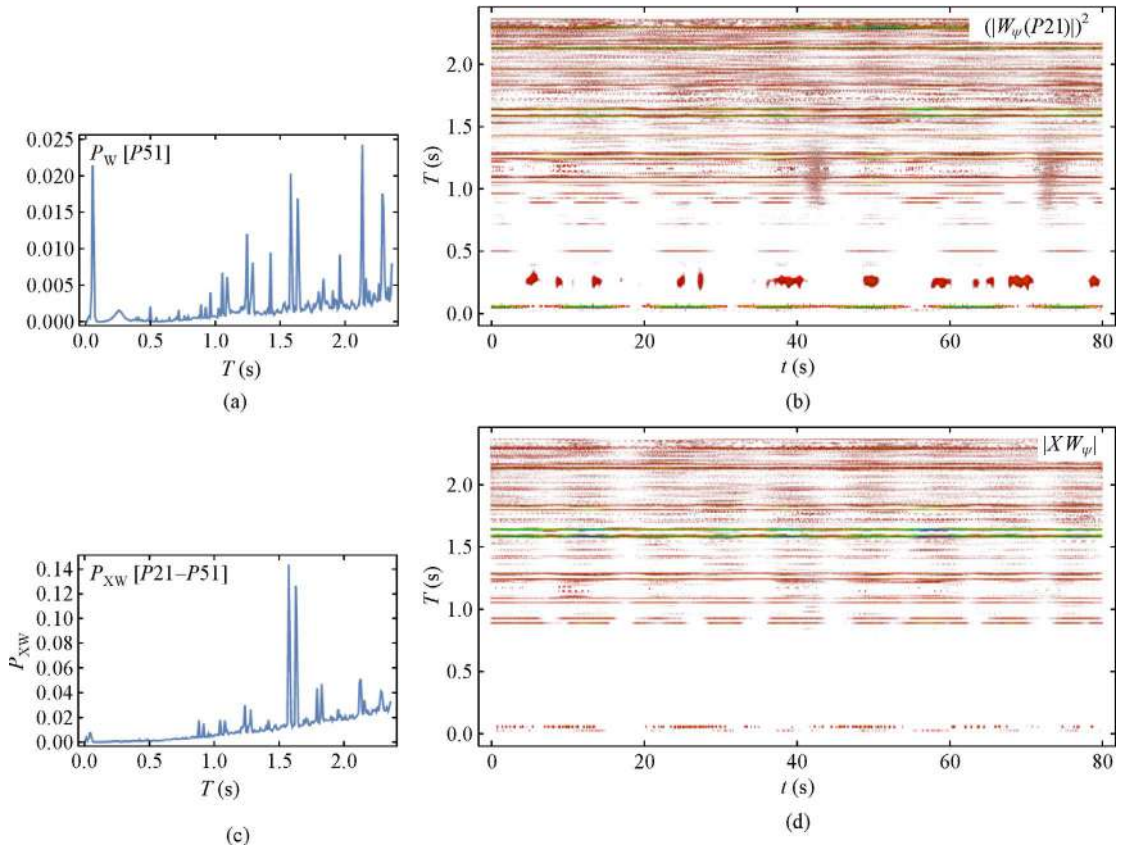

Fig. 15 Powers and energies of WTs of enhanced signals $P21$ and $P51$ and corresponding XWT and spectral power of XWT; plotted ranges are $0.02\text{Max}[|W_\psi|^2] \leqslant |W_\psi|^2 \leqslant \text{Max}[|W_\psi|^2]$ and $0.02\text{Max}[|W_\psi|] \leqslant |W_\psi| \leqslant \text{Max}[|W_\psi|]$. (a) The spectral power of the enhanced data $P51$, evaluated by $|W_\psi(P51)|^2$; (b) the density of energy for the enhanced data $P51$, $|W_\psi(P51)|^2$; (c) the spectral power of XWT for the enhanced data $P21$ and $P51$; (d) the density of $|XW_\psi|$ for the enhanced data $P21$ and $P51$.

enon if it is continuous through the time in the time-frequency representation, and has a local concentration of the spectral power in the frequency (scale) domain. This simultaneous study for different pairs of the enhanced data provides:

1) XWTs can improve the time-frequency representation for detection of excited frequencies (e.g., Fig. 15).

2) This transform, however, seems to be insufficient since there are several excited frequencies with continuous pattern through the time (see Figs. 14–16).

3) In this regard, the spectral power of WTs helps in capturing frequencies with considerable energies.

4) As the participation of higher modes is small (due to the stiffness of the structure), the multiresolution-based autocorrelation analysis can help distinguish such possible modal frequencies (Fig. 17).

5) XWTs can also decrease the effects of noise-like stochastic phenomena (see Fig. 15).

6) In detected periods, there are several couple of periods (near each other), because of the semi-symmetric plan of the structure (see Figs. 1 and 2).

Finally, the captured frequencies have been compared with those of a 3-D FE model; the results show a good agreement. Nevertheless, there are some frequencies which are not seen in the FE model, which can be justified by: 1) the absence of four narrow steel towers on the top of the main (concrete) tower in the FE model; 2) during the ambient vibration test, the main tower was in operation (this means some detected frequencies may correspond to the operating systems); 3) the operations of some equipment and fans on the main tower (which were not considered in the FE model); 4) the real tower has several localized damaged parts which were not considered in the FE model.

The detection algorithm used here is completely based on the signal processing approach. The results can be examined by other methods which take into account the structural properties (such as modal superposition in MDOFs) [13,19,76]. The identification of modal shapes and the corresponding damping will be studied in an independent work.

For future works, the following tasks are recommended:

1) Updating the FE model to include the damages and operating systems (mass and stiffness),

2) Using wavelet packets for the iterative enhancement approach. One of the shortcoming of the common discrete

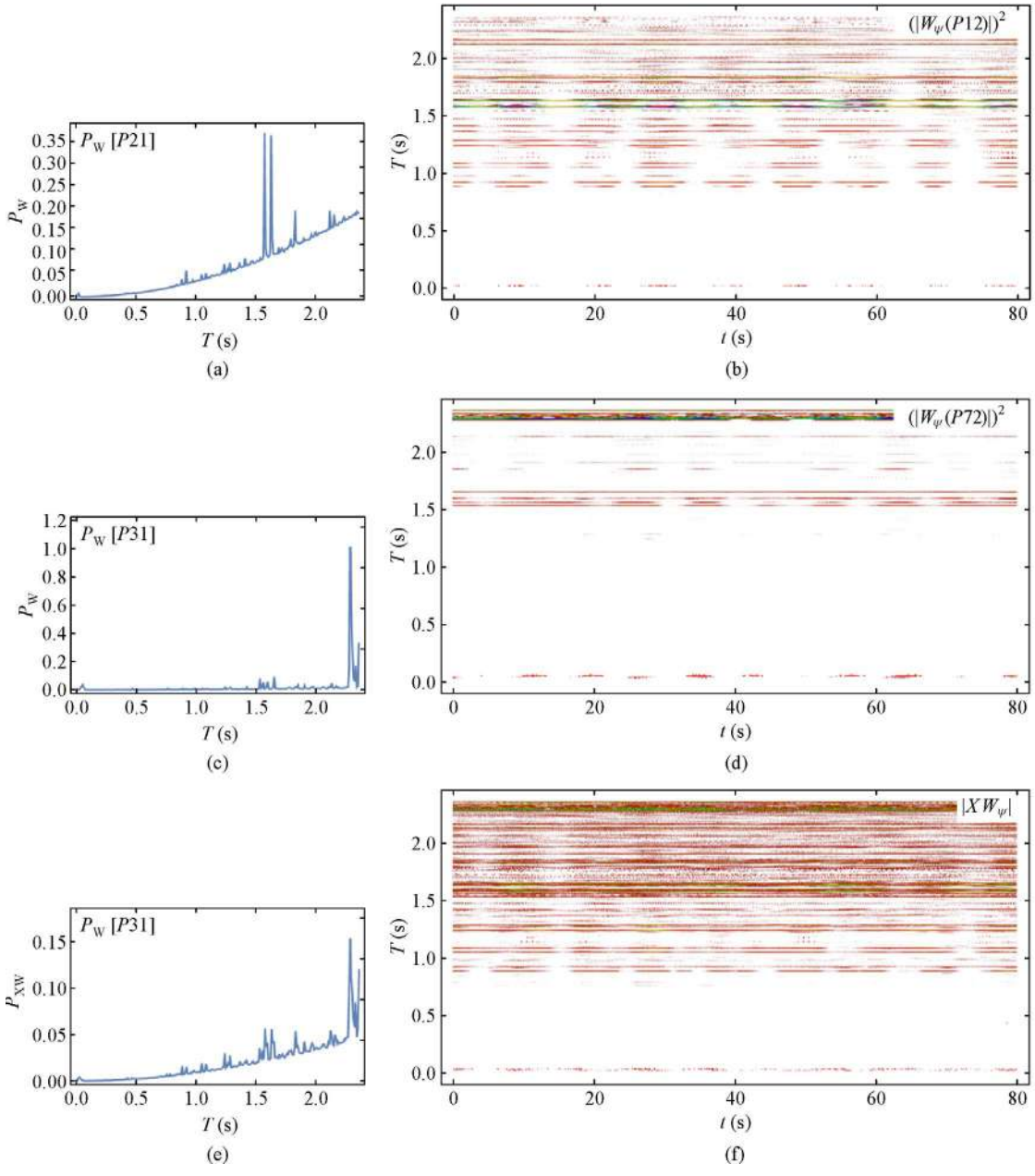

Fig. 16 Powers and energies of WTs of enhanced signals $P12$ & $P72$ and corresponding XWT and spectral power of XWT; plotted ranges are $0.02\text{Max}[|W_\psi|^2] \leqslant |W_\psi|^2 \leqslant \text{Max}[|W_\psi|^2]$ and $0.02\text{Max}[|W_\psi|] \leqslant |W_\psi| \leqslant \text{Max}[|W_\psi|]$. (a) The spectral power of the enhanced data $P12$, evaluated by $|W_\psi(12)|^2$; (b) the density of energy for the enhanced data $P12$, $|W_\psi(12)|^2$; (c) the spectral power of the enhanced data $P72$, evaluated by $|W_\psi(72)|^2$; (d) the density of energy for the enhanced data $P72$, $|W_\psi(72)|^2$; (e) the spectral power of XWT for the enhanced data $P12$ and $P72$; (f) the density of $|XW_\psi|$ for the enhanced data $P12$ and $P72$.

WTs is that they may not suitable for the processing of high frequency signals with nearly narrow bandwidth. For this reason, the wavelet packet was developed. The full transform leads to a large number of subbands (time-scale cells) and so significant numbers of signal representation possibilities. Decomposition increasing may lead to a more flexible analysis capability, especially, for data including different slow and fast variations. To capture properly these responses in the time-scale representations, the concept of the best basis was proposed. The best basis can be evaluated by defining a cost function where different ones were developed [118–120]. Hence, the best basis can depend on the cost definition. This dependency can also affect the iterative denoising results. This can also be considered for the future study.

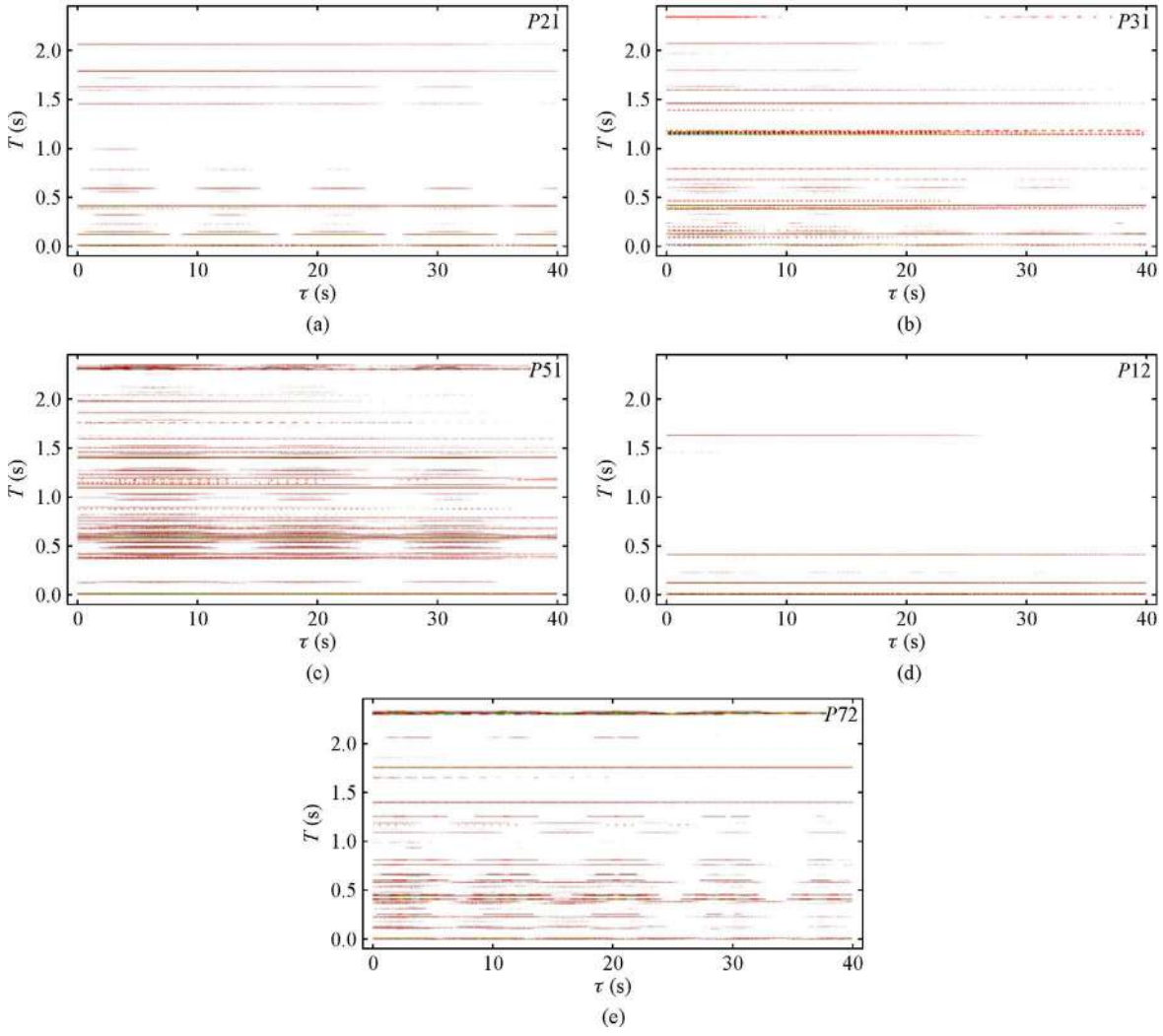

Fig. 17 Autocorrelations of wavelet coefficients of the enhanced data. (a) Results for the enhanced $P21$; (b) results for the enhanced $P31$; (c) results for the enhanced $P51$; (d) results for the enhanced $P12$; (e) results for the enhanced $P72$.

Table 8 Comparison of modal periods from the ambient vibration test and the FE model [117]

method	period (s)				
	0.0–0.5	0.5–1.0	1.0–1.5	1.5–2.0	2.0–2.5
the ambient vibration test	0.12, 0.4	0.88, 0.92	1.05, 1.24, 1.29	1.59, 1.64, 1.8, 1.84	2.12, 2.16, 2.3
the FE modelling	0.1829, 0.1843, 0.20, 0.2138, 0.3139, 0.3232, 0.3954, 0.4118	–	–	1.6004, 1.9738	–

Appendix A: Different thresholding approaches

The Universal, SURE, and GCV thresholding methods try to minimize the mean square error $MSE(\varepsilon)=\|f_\varepsilon - f\|^2/N_f$, where f_ε is a vector of thresholded data with the threshold value ε, f is the unknown smooth (untouched or without noise) data, and N_f denotes the length of data. Since f is unknown, it is necessary to estimate *MSE* [48]. In the Universal method, the threshold gives a minimax solution of the ideal mean squared error in the asymptotic behavior of *MSE* (as $N\to\infty$) [46–48,121]. In the SURE method, the Stein's unbiased risk estimator (SURE) is used for *MSE* estimations [46–48,122]. Asymptotically, the GCV function is a vertical translation of the MSE function, while the

GCV can be evaluated only based on input (noisy) data. Hence, the threshold value minimizing GCV also minimizes *MSE* [48].

Appendix B: Other approaches for parameter selection of the Morlet wavelet

Different approaches were suggested for selection of the pair $\{v_b, v_c\}$ for the Morlet wavelet for different purposes: 1) Obtaining an optimal time-frequency resolution based on the predefined modal frequencies $\{v_i\}$ of a structure in a way that two successive near modal frequencies can effectively be distinguishable [10]; 2) minimizing the Shannon entropy function; this wavelet entropy checks the sparsity of WT. Accordingly, a wavelet family with a minimum number of WT coefficients is the best [11]; 3) minimizing the end effect for the *i*th modal frequency, [10]; 4) maximizing the Kurtosis number, which measures the impulsive content (peakiness) of a signal [12]. These constraints can also be considered together. For example, Kijewski and Kareem [10] used the first and third conditions, while conditions 1 through 3 were satisfied in Ref. [13].

Appendix C: Denoising with variational-based minimization- the regularization approach

In the regularization approach, the denoised solution is the minimizer of the functional [58]: $Q(\boldsymbol{f}) = \rho(\boldsymbol{f}-\boldsymbol{y})^2 + \lambda \times \Omega(\boldsymbol{f})$; where: $\boldsymbol{y}$ and $\boldsymbol{f}$ denote noisy and denoised data, respectively; function $\rho(\boldsymbol{f}-\boldsymbol{y}) = \sqrt{\sum_i (f_i - y_i)^2}$ denotes the residual error; λ is a penaltization (smoothing) factor with possible values in the range of $0 \leqslant \lambda < \infty$; and function $\Omega(f)$ is an extra information. For this information, several measurements are available, such as: $\Omega(f)_{\mathrm{TV}} = \int |\mathrm{d}f/\mathrm{d}x| \mathrm{d}x$, $\Omega(f)_{L^2} = \int |\mathrm{d}^2 f/\mathrm{d}x^2|^2 \mathrm{d}x$ and $\Omega(f)_{\mathrm{Sobolev}} = \int |\mathrm{d}f/\mathrm{d}x + \mathrm{d}^2 f/\mathrm{d}x^2|^2 \mathrm{d}x$; where: $\Omega(f)_{\mathrm{TV}}$ measures the total variation (TV) of $f(x)$; $\Omega(f)_{L^2}$ and $\Omega(f)_{\mathrm{Sobolev}}$ are defined as semi-norms in the energy and Sobolev spaces, respectively. For numerical algorithms see Refs. [123–125].

To remap the possible range of λ into the unit range [0,1], the new parameter p can be defined as: $\lambda = \dfrac{1-p}{p}$. Cases $p \to 1$ and $p \to 0$ lead to data without denoising and a linear fit, respectively. Proper values for the parameter p can be estimated by the trial and error method or by an empirical approach, for example, by maximizing the *SNR*-*p* curve.

Acknowledgements The authors gratefully acknowledge the financial support of Iran National Science Foundation (INSF).

References

1. Doebling S W, Farrar C R, Prime M B. A summary review of vibration-based damage identification methods. Journal of Shock and Vibration, 1998, 30(2): 91–105
2. Doebling S W, Farrar C R, Prime M B, Shevitz D W. Damage Identification and Health Monitoring of Structural and Mechanical Systems from Changes in Their Vibration Characteristics: A Literature Review. OSTI.GOV Technical Report LA-13070-MS ON: DE96012168; TRN: 96:003834. 1996
3. Le T H, Tamura Y. Modal identification of ambient vibration structure using frequency domain decomposition and wavelet transform. In: Proceedings of the 7th Asia-Pacific Conference on Wind Engineering. Taipei, China: APCWE, 2009
4. Wijesundara K K, Negulescu C, Foerster E, Monfort Climent D. Estimation of modal properties of structures through ambient excitation measurements using continuous wavelet transform. In: Proceedings of 15WCEE. Lisbon: SPES, 2012, 26: 15–18
5. Abdel-Ghaffar A M, Scanlan R H. Ambient vibration studies of golden gate bridge: I. Suspended structure. Journal of Engineering Mechanics, 1985, 111(4): 463–482
6. Harik I, Allen D, Street R, Guo M, Graves R, Harison J, Gawry M. Free and ambient vibration of Brent-Spence Bridge. Journal of Structural Engineering, 1997, 123(9): 1262–1268
7. Farrar C, James G. System identification from ambient vibration measurements on a bridge. Journal of Sound and Vibration, 1997, 205(1): 1–18
8. Siringoringo D M, Fujino Y. System identification of suspension bridge from ambient vibration response. Engineering Structures, 2008, 30(2): 462–477
9. Sohn H. A Review of Structural Health Monitoring Literature: 1996–2001. Los Alamos National Laboratory Report. 2004
10. Kijewski T, Kareem A. Wavelet transforms for system identification in civil engineering. Computer-Aided Civil and Infrastructure Engineering, 2003, 18(5): 339–355
11. Lin J, Qu L. Feature extraction based on Morlet wavelet and its application for mechanical fault diagnosis. Journal of Sound and Vibration, 2000, 234(1): 135–148
12. Al-Raheem K F, Roy A, Ramachandran K P, Harrison D K, Grainger S. Rolling element bearing faults diagnosis based on autocorrelation of optimized: Wavelet de-noising technique. International Journal of Advanced Manufacturing Technology, 2009, 40(3–4): 393–402
13. Yan B, Miyamoto A, Brühwiler E. Wavelet transform-based modal parameter identification considering uncertainty. Journal of Sound and Vibration, 2006, 291(1–2): 285–301
14. Jiang X, Adeli H. Pseudospectra, MUSIC, and dynamic wavelet neural network for damage detection of highrise buildings. International Journal for Numerical Methods in Engineering, 2007, 71(5): 606–629
15. Osornio-Rios R A, Amezquita-Sanchez J P, Romero-Troncoso R J, Garcia-Perez A. MUSIC-ANN analysis for locating structural damages in a truss-type structure by means of vibrations. Computer-Aided Civil and Infrastructure Engineering, 2012, 27(9): 687–698

16. Carassale L, Percivale F. POD-based modal identification of wind-excited structures. In: Proceedings of the 12th International Conference on Wind Engineering. Cairns, 2007, 1239–1246
17. Tamura Y. Advanced Structural Wind Engineering. Tokyo: Springer, 2013, 347–376
18. Meo M, Zumpano G, Meng X, Cosser E, Roberts G, Dodson A. Measurements of dynamic properties of a medium span suspension bridge by using the wavelet transforms. Mechanical Systems and Signal Processing, 2006, 20(5): 1112–1133
19. Lardies J, Gouttebroze S. Identification of modal parameters using the wavelet transform. International Journal of Mechanical Sciences, 2002, 44(11): 2263–2283
20. He X, Moaveni B, Conte J P, Elgamal A, Masri S F. Modal identification study of Vincent Thomas bridge using simulated wind-induced ambient vibration data. Computer-Aided Civil and Infrastructure Engineering, 2008, 23(5): 373–388
21. Ni Y C, Lu X L, Lu W S. Field dynamic test and Bayesian modal identification of a special structure—The Palms Together Dagoba. Structural Control and Health Monitoring, 2016, 23(5): 838–856
22. Zhang F L, Ventura C E, Xiong H B, Lu W S, Pan Y X, Cao J X. Evaluation of the dynamic characteristics of a super tall building using data from ambient vibration and shake table tests by a Bayesian approach. Structural Control and Health Monitoring, 2017, 25(2): 1– 18
23. Kang N, Kim H, Sunyoung Choi & Seongwoo Jo, Hwang J S, Yu E. Performance evaluation of TMD under typhoon using system identification and inverse wind load estimation. Computer-Aided Civil and Infrastructure Engineering, 2012, 27(6): 455–473
24. Wenzel H, Pichler D. Ambient Vibration Monitoring. Vienna: John Wiley & Sons, 2005
25. Brownjohn J M W. Structural health monitoring of civil infrastructure. Philosophical Transactions of the Royal Society A, 2007, 365(1851): 589–622
26. He X H, Hua X G, Chen Z Q, Huang F L. EMD-based random decrement technique for modal parameter identification of an existing railway bridge. Engineering Structures, 2011, 33(4): 1348–1356
27. Huang C S, Hung S L, Lin C I, Su W C. A wavelet-based approach to identifying structural modal parameters from seismic response and free vibration data. Computer-Aided Civil and Infrastructure Engineering, 2005, 20(6): 408–423
28. Ivanovic S, Trifunac M D, Novikova E I, Gladkov A A, Todorovska M I. Instrumented 7-Storey Reinforced Concrete Building in Van Nuys, California: Ambient Vibration Survey Following the Damage from the 1994 Northridge Earthquake. Report No. CE 9903. 1999
29. Ivanovic S S, Trifunac M D, Todorovska M I. Ambient vibration tests of structures—A review. ISET Journal of Earthquake Technology, 2000, 37: 165–197
30. Brownjohn J M W, De Stefano A, Xu Y L, Wenzel H, Aktan A E. Vibration-based monitoring of civil infrastructure: Challenges and successes. Journal of Civil Structural Health Monitoring, 2011, 1(3–4): 79–95
31. Roeck G D. The state-of-the-art of damage detection by vibration monitoring: The SIMCES experience. Structural Control and Health Monitoring, 2003, 10(2): 127–134
32. He D, Wang X, Friswell M I, Lin J. Identification of modal parameters from noisy transient response signals. Structural Control and Health Monitoring, 2017, 24(11): 1–10
33. Juang J N, Pappa R S. Effects of noise on modal parameters identified by the eigensystem realization algorithm. Journal of Guidance, Control, and Dynamics, 1986, 9(3): 294–303
34. Dorvash S, Pakzad S N. Effects of measurement noise on modal parameter identification. Smart Materials and Structures, 2012, 21(6): 065008
35. Li P, Hu S L J, Li H J. Noise issues of modal identification using eigensystem realization algorithm. Procedia Engineering, 2011, 14: 1681–1689
36. Yoshitomi S, Takewaki I. Noise-effect compensation method for physical-parameter system identification under stationary random input. Structural Control and Health Monitoring, 2009, 16(3): 350–373
37. Huang C S, Su W C. Identification of modal parameters of a time invariant linear system by continuous wavelet transformation. Mechanical Systems and Signal Processing, 2007, 21(4): 1642–1664
38. Yan B, Miyamoto A. A comparative study of modal parameter identification based on wavelet and Hilbert-Huang transforms. Computer-Aided Civil and Infrastructure Engineering, 2006, 21(1): 9–23
39. Su W C, Huang C S, Chen C H, Liu C Y, Huang H C, Le Q T. Identifying the modal parameters of a structure from ambient vibration data via the stationary wavelet packet. Computer-Aided Civil and Infrastructure Engineering, 2014, 29(10): 738–757
40. Su W C, Liu C Y, Huang C S. Identification of instantaneous modal parameter of time-varying systems via a wavelet-based approach and its application. Computer-Aided Civil and Infrastructure Engineering, 2014, 29(4): 279–298
41. Chen S L, Liu J J, Lai H C. Wavelet analysis for identification of damping ratios and natural frequencies. Journal of Sound and Vibration, 2009, 323(1–2): 130–147
42. Yi T H, Li H N, Zhao X Y. Noise smoothing for structural vibration test signals using an improved wavelet thresholding technique. Sensors (Basel), 2012, 12(8): 11205–11220
43. Huang N E. Hilbert-Huang Transform and its Applications. Singapore: World Scientific, 2011, 1–26
44. Teolis A. Computational Signal Processing with Wavelets. Basel: Springer Science & Business Media, 2012
45. Misiti M, Misiti Y, Oppenheim G, Poggi J M. Wavelets and their Applications. Wiltshire: John Wiley & Sons, 2013
46. Mallat S. Wavelet Analysis & Its Applications. London: Academic Press, 1999
47. Van Fleet P. Discrete Wavelet Transformations: An Elementary Approach with Applications. New Jersey: John Wiley & Sons, 2011
48. Jansen M. Noise Reduction by Wavelet Thresholding. New York: Springer Science & Business Media, 2012
49. Soman K P. Insight into Wavelets: From Theory to Practice. New Delhi: PHI Learning Pvt. Ltd., 2010
50. Jiang X, Mahadevan S, Adeli H. Bayesian wavelet packet denoising for structural system identification. Structural Control and Health Monitoring, 2007, 14(2): 333–356

51. Coifman R R, Wickerhauser M V. Adapted waveform “de-Noising” for medical signals and images. IEEE Engineering in Medicine and Biology Magazine, 1995, 14(5): 578–586
52. Coifman R R, Wickerhauser M V. Experiments with adapted wavelet de-noising for medical signals and images. In: Time Frequency and Wavelets in Biomedical Signal Processing, IEEE press series in Biomedical Engineering. New York: Wiley-IEEE Press, 1998
53. Hadjileontiadis L J, Panas S M. Separation of discontinuous adventitious sounds from vesicular sounds using a wavelet-based filter. IEEE Transactions on Biomedical Engineering, 1997, 44(12): 1269–1281
54. Hadjileontiadis L J, Liatsos C N, Mavrogiannis C C, Rokkas T A, Panas S M. Enhancement of bowel sounds by wavelet-based filtering. IEEE Transactions on Biomedical Engineering, 2000, 47(7): 876–886
55. Ranta R, Heinrich C, Louis-Dorr V, Wolf D. Interpretation and improvement of an iterative wavelet-based denoising method. IEEE Signal Processing Letters, 2003, 10(8): 239–241
56. Ranta R, Louis-Dorr V, Heinrich C, Wolf D. Iterative wavelet-based denoising methods and robust outlier detection. IEEE Signal Processing Letters, 2005, 12(8): 557–560
57. Starck J L, Bijaoui A. Filtering and deconvolution by the wavelet transform. Signal Processing, 1994, 35(3): 195–211
58. Peyré G. Advanced Signal, Image and Surface Processing-Numerical Tours. Université Paris-Dauphine, 2010
59. Grinsted A, Moore J C, Jevrejeva S. Application of the cross wavelet transform and wavelet coherence to geophysical time series. Nonlinear Processes in Geophysics, 2004, 11(5/6): 561–566
60. Rafiee J, Tse P W. Use of autocorrelation of wavelet coefficients for fault diagnosis. Mechanical Systems and Signal Processing, 2009, 23(5): 1554–1572
61. Jiang X, Adeli H. Wavelet packet-autocorrelation function method for traffic flow pattern analysis. Computer-Aided Civil and Infrastructure Engineering, 2004, 19(5): 324–337
62. Bruns A. Fourier-, Hilbert-and wavelet-based signal analysis: Are they really different approaches? Journal of Neuroscience Methods, 2004, 137(2): 321–332
63. Le Van Quyen M, Foucher J, Lachaux J P, Rodriguez E, Lutz A, Martinerie J, Varela F J. Comparison of Hilbert transform and wavelet methods for the analysis of neuronal synchrony. Journal of Neuroscience Methods, 2001, 111(2): 83–98
64. Rainieri C, Fabbrocino G. Operational Modal Analysis of Civil Engineering Structures. New York: Springer, 2014
65. Brownjohn J M W. Ambient vibration studies for system identification of tall buildings. Earthquake Engineering & Structural Dynamics, 2003, 32(1): 71–95
66. Mahato S, Teja M V, Chakraborty A. Adaptive HHT (AHHT) based modal parameter estimation from limited measurements of an RC-framed building under multi-component earthquake excitations. Structural Control and Health Monitoring, 2015, 22(7): 984–1001
67. Peng Z K, Tse P W, Chu F L. An improved Hilbert–Huang transform and its application in vibration signal analysis. Journal of Sound and Vibration, 2005, 286(1–2): 187–205
68. Yang W X. Interpretation of mechanical signals using an improved Hilbert-Huang transform. Mechanical Systems and Signal Processing, 2008, 22(5): 1061–1071
69. Bao C, Hao H, Li Z X, Zhu X. Time-varying system identification using a newly improved HHT algorithm. Computers & Structures, 2009, 87(23–24): 1611–1623
70. Wu Z, Huang N E. Ensemble empirical mode decomposition: A noise-assisted data analysis method. Advances in Data Science and Adaptive Analysis, 2009, 1(1): 1–41
71. Daubechies I, Lu J, Wu H T. Synchrosqueezed wavelet transforms: An empirical mode decomposition-like tool. Applied and Computational Harmonic Analysis, 2011, 30(2): 243–261
72. Brevdo E, Wu H T, Thakur G, Fuckar N S. Synchrosqueezing and its applications in the analysis of signals with time-varying spectrum. Proceedings of the National Academy of Sciences of the United States of America, 2011, 93: 1079–1094
73. Perez-Ramirez C A, Amezquita-Sanchez J P, Adeli H, Valtierra-Rodriguez M, Camarena-Martinez D, Romero-Troncoso R J. New methodology for modal parameters identification of smart civil structures using ambient vibrations and synchrosqueezed wavelet transform. Engineering Applications of Artificial Intelligence, 2016, 48: 1–12
74. Li C, Liang M. Time-frequency signal analysis for gearbox fault diagnosis using a generalized synchrosqueezing transform. Mechanical Systems and Signal Processing, 2012, 26: 205–217
75. Feng Z, Chen X, Liang M. Iterative generalized synchrosqueezing transform for fault diagnosis of wind turbine planetary gearbox under nonstationary conditions. Mechanical Systems and Signal Processing, 2015, 52–53: 360–375
76. Staszewski W J. Identification of damping in MDOF systems using time-scale decomposition. Journal of Sound and Vibration, 1997, 203(2): 283–305
77. Areias P, Rabczuk T, Camanho P. Finite strain fracture of 2D problems with injected anisotropic softening elements. Theoretical and Applied Fracture Mechanics, 2014, 72: 50–63
78. Nanthakumar S, Lahmer T, Zhuang X, Zi G, Rabczuk T. Detection of material interfaces using a regularized level set method in piezoelectric structures. Inverse Problems in Science and Engineering, 2016, 24(1): 153–176
79. Hamdia K M, Silani M, Zhuang X, He P, Rabczuk T. Stochastic analysis of the fracture toughness of polymeric nanoparticle composites using polynomial chaos expansions. International Journal of Fracture, 2017, 206(2): 215–227
80. Hamdia K M, Ghasemi H, Zhuang X, Alajlan N, Rabczuk T. Sensitivity and uncertainty analysis for flexoelectric nanostructures. Computer Methods in Applied Mechanics and Engineering, 2018, 337: 95–109
81. Vu-Bac N, Lahmer T, Zhuang X, Nguyen-Thoi T, Rabczuk T. A software framework for probabilistic sensitivity analysis for computationally expensive models. Advances in Engineering Software, 2016, 100: 19–31
82. Areias P, Rabczuk T, Dias-da-Costa D. Element-wise fracture algorithm based on rotation of edges. Engineering Fracture Mechanics, 2013, 110: 113–137
83. Areias P, Rabczuk T. Finite strain fracture of plates and shells with configurational forces and edge rotations. International Journal for Numerical Methods in Engineering, 2013, 94(12): 1099–1122

84. Areias P, Msekh M, Rabczuk T. Damage and fracture algorithm using the screened Poisson equation and local remeshing. Engineering Fracture Mechanics, 2016, 158: 116–143
85. Areias P, Rabczuk T. Steiner-point free edge cutting of tetrahedral meshes with applications in fracture. Finite Elements in Analysis and Design, 2017, 132: 27–41
86. Areias P, Reinoso J, Camanho P P, César de Sá J, Rabczuk T. Effective 2D and 3D crack propagation with local mesh refinement and the screened Poisson equation. Engineering Fracture Mechanics, 2018, 189: 339–360
87. Anitescu C, Hossain M N, Rabczuk T. Recovery-based error estimation and adaptivity using high-order splines over hierarchical T-meshes. Computer Methods in Applied Mechanics and Engineering, 2018, 328: 638–662
88. Chau-Dinh T, Zi G, Lee P S, Rabczuk T, Song J H. Phantom-node method for shell models with arbitrary cracks. Computers & Structures, 2012, 92–93: 242–256
89. Budarapu P R, Gracie R, Bordas S P, Rabczuk T. An adaptive multiscale method for quasi-static crack growth. Computational Mechanics, 2014, 53(6): 1129–1148
90. Talebi H, Silani M, Bordas S P, Kerfriden P, Rabczuk T. A computational library for multiscale modeling of material failure. Computational Mechanics, 2014, 53(5): 1047–1071
91. Budarapu P R, Gracie R, Yang S W, Zhuang X, Rabczuk T. Efficient coarse graining in multiscale modeling of fracture. Theoretical and Applied Fracture Mechanics, 2014, 69: 126–143
92. Talebi H, Silani M, Rabczuk T. Concurrent multiscale modeling of three dimensional crack and dislocation propagation. Advances in Engineering Software, 2015, 80: 82–92
93. Amiri F, Millán D, Shen Y, Rabczuk T, Arroyo M. Phase-field modeling of fracture in linear thin shells. Theoretical and Applied Fracture Mechanics, 2014, 69: 102–109
94. Areias P, Rabczuk T, Msekh M. Phase-field analysis of finite-strain plates and shells including element subdivision. Computer Methods in Applied Mechanics and Engineering, 2016, 312: 322–350
95. Ren H, Zhuang X, Cai Y, Rabczuk T. Dual-horizon peridynamics. International Journal for Numerical Methods in Engineering, 2016, 108(12): 1451–1476
96. Ren H, Zhuang X, Rabczuk T. Dual-horizon peridynamics: A stable solution to varying horizons. Computer Methods in Applied Mechanics and Engineering, 2017, 318: 762–782
97. Rabczuk T, Areias P, Belytschko T. A meshfree thin shell method for non-linear dynamic fracture. International Journal for Numerical Methods in Engineering, 2007, 72(5): 524–548
98. Rabczuk T, Belytschko T. A three-dimensional large deformation meshfree method for arbitrary evolving cracks. Computer Methods in Applied Mechanics and Engineering, 2007, 196(29–30): 2777–2799
99. Rabczuk T, Gracie R, Song J H, Belytschko T. Immersed particle method for fluid-structure interaction. International Journal for Numerical Methods in Engineering, 2010, 81: 48–71
100. Rabczuk T, Bordas S, Zi G. On three-dimensional modelling of crack growth using partition of unity methods. Computers & Structures, 2010, 88(23–24): 1391–1411
101. Rabczuk T, Zi G, Bordas S, Nguyen-Xuan H. A simple and robust three-dimensional cracking-particle method without enrichment. Computer Methods in Applied Mechanics and Engineering, 2010, 199(37–40): 2437–2455
102. Rabczuk T, Belytschko T. Cracking particles: A simplified meshfree method for arbitrary evolving cracks. International Journal for Numerical Methods in Engineering, 2004, 61(13): 2316–2343
103. Rabczuk T, Belytschko T, Xiao S. Stable particle methods based on Lagrangian kernels. Computer Methods in Applied Mechanics and Engineering, 2004, 193(12–14): 1035–1063
104. Amiri F, Anitescu C, Arroyo M, Bordas S P A, Rabczuk T. XLME interpolants, a seamless bridge between XFEM and enriched meshless methods. Computational Mechanics, 2014, 53(1): 45–57
105. Hughes T J, Cottrell J A, Bazilevs Y. Isogeometric analysis: CAD, finite elements, NURBS, exact geometry and mesh refinement. Computer Methods in Applied Mechanics and Engineering, 2005, 194(39–41): 4135–4195
106. Nguyen-Thanh N, Nguyen-Xuan H, Bordas S P A, Rabczuk T. Isogeometric analysis using polynomial splines over hierarchical T-meshes for two-dimensional elastic solids. Computer Methods in Applied Mechanics and Engineering, 2011, 200(21–22): 1892–1908
107. Nguyen V P, Anitescu C, Bordas S P, Rabczuk T. Isogeometric analysis: An overview and computer implementation aspects. Mathematics and Computers in Simulation, 2015, 117: 89–116
108. Ghasemi H, Park H S, Rabczuk T. A level-set based IGA formulation for topology optimization of flexoelectric materials. Computer Methods in Applied Mechanics and Engineering, 2017, 313: 239–258
109. Nguyen-Thanh N, Kiendl J, Nguyen-Xuan H, Wüchner R, Bletzinger K U, Bazilevs Y, Rabczuk T. Rotation free isogeometric thin shell analysis using PHT-splines. Computer Methods in Applied Mechanics and Engineering, 2011, 200(47–48): 3410–3424
110. Nguyen-Thanh N, Valizadeh N, Nguyen M, Nguyen-Xuan H, Zhuang X, Areias P, Zi G, Bazilevs Y, De Lorenzis L, Rabczuk T. An extended isogeometric thin shell analysis based on Kirchhoff-Love theory. Computer Methods in Applied Mechanics and Engineering, 2015, 284: 265–291
111. Nguyen-Thanh N, Zhou K, Zhuang X, Areias P, Nguyen-Xuan H, Bazilevs Y, Rabczuk T. Isogeometric analysis of large-deformation thin shells using RHT-splines for multiple-patch coupling. Computer Methods in Applied Mechanics and Engineering, 2017, 316: 1157–1178
112. Vu-Bac N, Duong T, Lahmer T, Zhuang X, Sauer R, Park H, Rabczuk T. A NURBS-based inverse analysis for reconstruction of nonlinear deformations of thin shell structures. Computer Methods in Applied Mechanics and Engineering, 2018, 331: 427–455
113. Ghasemi H, Park H S, Rabczuk T. A multi-material level set-based topology optimization of flexoelectric composites. Computer Methods in Applied Mechanics and Engineering, 2018, 332: 47–62
114. Ghorashi S S, Valizadeh N, Mohammadi S, Rabczuk T. T-spline based XIGA for fracture analysis of orthotropic media. Computers & Structures, 2015, 147: 138–146
115. Kumari S, Vijay R. Effect of symlet filter order on denoising of still

images. Advances in Computers, 2012, 3(1): 137–143
116. Rousseeuw P J, Leroy A M. Robust Regression & Outlier Detection. Hoboken: John Wiley & Sons, 1987
117. Samadi J. Seismic Behavior of structure-equipment in a petrochemical complex to evaluate vulnerability assessment: A case study. Thesis for the Master's Degree. Tehran: Civil Engineering, University of Tehran, 2010
118. Jensen A, la Cour-Harbo A. Ripples in Mathematics: The Discrete Wavelet Transform. Heidelberg: Springer Science & Business Media, 2001
119. Soman K. Insight into Wavelets: From Theory to Practice. New Delhi: PHI Learning Pvt. Ltd., 2010
120. Wickerhauser M V. Adapted Wavelet Analysis: From Theory to Software. Natick: AK Peters/CRC Press, 1996
121. Donoho D L, Johnstone J M. Ideal spatial adaptation by wavelet shrinkage. Biometrika, 1994, 81(3): 425–455
122. Stein C M. Estimation of the mean of a multivariate normal distribution. Annals of Statistics, 1981, 9(6): 1135–1151
123. Yousefi H, Ghorashi S S, Rabczuk T. Directly simulation of second order hyperbolic systems in second order form via the regularization concept. Communications in Computational Physics, 2016, 20(1): 86–135
124. Yousefi H, Noorzad A, Farjoodi J. Multiresolution based adaptive schemes for second order hyperbolic PDEs in elastodynamic problems. Applied Mathematical Modelling, 2013, 37(12–13): 7095–7127
125. Selesnick I W, Bayram I. Total Variation Filtering, White paper, Connexions Web site. 2010